NIST Technical Note 2087

Smoldering Propensity in Upholstered Furniture: Using Computational and Experimental Methods to Aid the Selection of an Appropriate Smoldering Scenario

Jiuling Yang
Guillermo Rein
Haixiang Chen
Mauro Zammarano

This publication is available free of charge from:
https://doi.org/10.6028/NIST.TN.2087

National Institute of
Standards and Technology
U.S. Department of Commerce

NIST Technical Note 2087

Smoldering Propensity in Upholstered Furniture: Using Computational and Experimental Methods to Aid the Selection of an Appropriate Smoldering Scenario

Jiuling Yang
Mauro Zammarano
Fire Research Division
Engineering Laboratory

Guillermo Rein
Department of Mechanical Engineering
Imperial College London

Haixiang Chen
State Key Laboratory of Fire Science
University of Science and Technology of China

This publication is available free of charge from:
https://doi.org/10.6028/NIST.TN.2087

February 2020

U.S. Department of Commerce
Wilbur L. Ross, Jr., Secretary

National Institute of Standards and Technology
Walter Copan, NIST Director and Undersecretary of Commerce for Standards and Technology

National Institute of Standards and Technology Technical Note 2087
Natl. Inst. Stand. Technol. Tech. Note 2087, 44 pages (February 2020)
CODEN: NTNOEF

This publication is available free of charge from:
https://doi.org/10.6028/NIST.TN.2087

Abstract

Reduced-scale mock-ups had been developed to assess and regulate smoldering ignition resistance of residential upholstered furniture (RUF). However, there are limited data available on the effect of the mock-up test configuration on smoldering propensity and how it affects the degree of correlation with full-scale performance. In this work, the smoldering propensity for standard mock-ups (SMs, where the foam is in contact with a support frame) and modified mock-ups (MMs, where an air gap is introduced between the foam and the frame), were computationally simulated and compared to experimental results. Experimental data showed an up to a four-fold increase in smoldering mass loss in a MM as compared to a SM for a test time of 35 min with a 51 mm-thick foam. The model results indicated that the buoyant airflow at the bottom of the mock-up was enhanced in the MM, giving rise to a higher foam oxidation rate, a higher peak smoldering temperature and higher mass loss rate as compared to the SM, and; that oxygen supply was dominated by diffusion-driven transport from the boundaries in proximity of the heating source in the SM. Additionally, the effects of foam thickness on smoldering propensity were studied experimentally and numerically with foam thicknesses of 51 mm (2 inch) and 76 mm (3 inch). With an increase in the foam thickness, the smoldering propensity is weakened in the MM but enhanced in the SM. The model was able to predict the ranking of smoldering propensity quantified by the mass loss in experiments: $ML(t)_{SM2} < ML(t)_{SM3} < ML(t)_{MM3} < ML(t)_{MM2}$, where ML_{SM2} is the mass loss (ML) with a 51 mm-thick foam in SM, ML_{SM3} is the ML with a 76 mm-thick foam in SM, ML_{MM3} is the ML with a 76 mm-thick foam in MM and ML_{MM2} is the ML with a 51 mm-thick foam in MM. These results indicate that reduced-scale tests based on SM2 tends to underpredict smoldering propensity and that MM2 may offer a near-worst-case scenario, useful to identify the upholstery materials that prevent most smoldering ignitions independent of the construction and geometry of the actual furniture.

Key words

Buoyant airflow; Computational model; Flexible polyurethane foam; Smoldering propensity

Table of Contents

List of Tables

List of Figures

Nomenclature

Letters		*Greek symbols*	
A	pre-exponential factor (s^{-1})	α	thermal diffusivity ($m^2\ s^{-1}$)
c	specific heat capacity ($J\ kg^{-1}\ K^{-1}$)	ε	emissivity
d/d_f	foam thickness (mm)/fiber diameter (mm)	β	volumetric thermal expansion coefficient (K^{-1})
D	diffusivity ($m^2\ s^{-1}$)	$\dot{\omega}'''$	non-dimensional reaction rate (s^{-1})
E	activation energy ($kJ\ mol^{-1}$)	ν	mass yield
g	gravitational acceleration ($m\ s^{-2}$)	φ	porosity
h_c	convective heat transfer coefficient ($W\ m^{-2}\ K^{-1}$)	μ	dynamic viscosity ($kg\ m^{-1}\ s^{-1}$)
h_m	mass transfer coefficient ($kg\ m^{-2}\ s^{-1}$)	ρ	density ($kg\ m^{-3}$)
h_{sg}	volumetric heat transfer coefficient ($W\ m^{-3}\ K^{-1}$)	σ	Stefan-Boltzmann constant ($W\ m^{-2}\ K^{-4}$)
ΔH	heat release ($J\ g^{-1}$)	*subscripts*	
k	thermal conductivity ($W\ m^{-1}\ K^{-1}$)	$0, \infty$	initial, ambient
K	permeability (m^2)	*A/a*	reactant species/ash
Le	Lewis number	*c/co/con*	char/char oxidation/convective
m	mass (kg)	*d/dff*	depletion /diffusive
M	molecular mass ($g\ mol^{-1}$)	*eff*	effective coefficient
MM	modified mock-up	*f /fo/fp*	formation/foam/foam oxidation/ foam pyrolysis
MLR	mass loss rate ($kg\ m^{-3}\ s^{-1}$)	*g/gp*	gas phase/gas products
n/N	reaction order/node number	*i/ig*	solid species *i* /ignition
p	pressure (Pa)	*j*	gas species *j*
$\dot{q}''$	heat flux ($W\ m^{-2}$)	*k*	heterogeneous reaction *k*
R	universal gas constant ($J\ mol^{-1}\ K^{-1}$)	*mix*	gas mixture
SM	standard mock-up	*r*	radius
T	temperature (°C)	*s*	solid phase
$\mathbf{u}$	velocity vector ($m\ s^{-1}$)	*superscripts*	
x	*x* coordinate (mm)	(-)	weighted or averaged
X	volume fraction		
y	*y* coordinate (mm)/ mass fraction (m_i/m_0)		

1. Introduction

Smoldering is a self-sustaining heterogeneous oxidation reaction that induces a slow, low temperature, flameless combustion [1]. Smoldering constitutes a potential threat to human's life and property safety for two main reasons. First, it produces potentially deadly amounts of carbon monoxide at a higher yield (even though at a slower rate) as compared to flaming combustion. Second, smoldering can induce flaming ignition via smoldering-to-flaming transition with heat sources otherwise too weak to directly cause flaming ignition [2]. Flexible polyurethane foam (FPUF) is the most commonly used padding material for residential upholstered furniture (RUF). FPUF is a smoldering-prone material due to a prevalently open cell structure that gives a combination of low-density, low thermal conductivity, high surface to volume ratio, and high oxygen transport through the FPUF [3].

Fires involving in RUF frequently grow very rapidly and reach high heat release rates. As a result, fires involving in RUF are the single largest cause of civilian deaths in U.S. home fires (about 24%) with a yearly estimated average of 610 deaths, 8900 fires, 1120 injuries and $566 million in direct damage [4]. Fires in spaces containing RUF are roughly eleven time more likely to be fatal than fires elsewhere in a residence. Smoldering ignition due to smoking materials (*i.e.*, cigarettes and other tobacco products) is the leading ignition source in RUF fires [5].

In order to assess cigarette ignition resistance of RUF, reduced-scale tests (*e.g.*, UFAC [6], ASTM E1353 [7], NFPA 260 [8]) (TB117-2013 [9]) have been developed in the U.S. from that firstly designed by the National Institute of Standards and Technology (NIST) (formerly the National Bureau of Standards, NBS) [10]. These tests are all based on the same test configuration that will be referred to as standard mock-ups (SMs) in the remainder of the paper. In the SMs, two pieces of FPUFs are placed vertically and horizontally at right angles to one another. The foam thickness is usually between 51 mm (2 inch) and 76 mm (3 inch). The two pieces of FPUF are held in tight contact with a wooden frame (on the bottom and substantial areas of the front and back) and are covered with upholstery material. A cigarette ignition source is placed along the crevice formed by the two pieces of FPUFs. This test configuration is based on a "sectional approach" that aims to simulate the section of a RUF item with the highest likelihood of smoldering ignition, *i.e.*, the junction formed by a seat (horizontal) and back (vertical) cushions.

In the absence of a federal regulation, California Technical Bulletin TB 117-2013 has become a *de-facto* national standard [9]. On May 2019, a bill to adopt TB117-2013 as a Federal flammability standard was proposed and on December 2019, it was passed in the House [11]. In the 1990s, Damant [12] reported a comprehensive study comparing smoldering propensity of finished furniture products (according to California Technical Bulletin TB 116 [13]) and the smoldering behavior of reduced-scale tests (using a test configuration identical to TB117-2013 mimicking the seat/back and seat/arm crevices of the RUF items). Damant found that, out of 100 randomly selected chairs, 80 chairs passed TB 116 (*i.e.*, no transition to flaming and char propagation distance from the cigarette less than 50 mm) and 20 chairs failed. The RUF material combinations used in these 80 chairs that passed TB 116 also passed the reduced-scale test (*i.e.*, no sustained smoldering). However, of the 20 RUF material combinations that failed TB 116, only 12 failed the reduced-scale test in a seat/back or seat/arm crevice configuration, 7 passed, and one was not tested. In other words, the standard bench-scale test never failed to deem "good" chairs at real-scale (*i.e.*, no false positives) but did deem "good" chairs that developed sustained smoldering at real-scale (*i.e.*, false negatives) in about (37 to 40) % of the cases. This is an indication that the reduced-scale tests based on the standard mock-up with a 51 mm thick foam, like TB 117-2013, underestimate the smoldering propensity of actual RUF. Similarly, the Consumer Product Safety Commission (CPSC) [14] observed that some combinations of upholstery materials led to sustained smoldering in real-scale RUF mock-ups and non-sustained smoldering in the standard mock-up configuration with a foam thickness of 76 mm.

Smoldering is an oxygen-limited reaction and the smoldering spread rate is directly proportional to the oxygen flow through the smoldering zone [15]. Recently, Zammarano *et al.* [16] speculated that in the standard mock-up test buoyancy-driven convection and diffusion would be suppressed to a large extent because a large fraction of the mock-up surface was in contact with the wooden frame. As a result, oxygen supply to the smoldering front would be suppressed and the smoldering spread rate would be decreased as compared to configurations where the air flow was unencumbered. To support this hypothesis, they designed a modified reduced-scale mock-up where an air gap between the foam and the wooden frame was added. They observed an up to three-fold increase in the smoldering propensity (measured as mass loss) in the modified mock-up (MM) as compared to the standard mock-up (SM) on a 76 mm-thick foam.

In this study, we further investigate the effects of the mock-up test configuration on smoldering propensity by: (1) collecting additional experimental data for SMs and MMs using 51 mm-thick and 76 mm-thick foams, and; (2) by developing a novel two-dimensional (2-D) computational model that provides insights into the effects of test configuration on oxygen supply during smoldering. This model is an extension of previous one-dimensional (1-D) models for FPUF smoldering described in [15, 17-20]. Computational 1-D models have been developed using 2-step [15], 3-step [17, 18, 20] or an improved 5-step [19] reaction schemes. One study extended such studies to two-dimensions using a 7-step reaction scheme [21]. All of these models only considered the smoldering behavior under forced airflow or under microgravity where the effects of buoyant airflow could be ignored. The 2-D computational model proposed here accounts for both buoyant airflow and diffusion of the air supply. It is used to investigate the mechanisms by which mock-up access to air and/or foam thickness affect smoldering.

2. Experimental Section[1]

2.1. Materials

All materials were used as received unless otherwise indicated. One type of FPUF (open - cell, no fire retardants) and one cover fabric were selected. The FPUF met the specifications prescribed for standard polyurethane foam in TB117-2013 [9]. The cover fabric was a 100 % cotton denim with an average surface density of (445 ± 3) g m^{-2}. A cigarette (NIST SRM 1196)

---

[1] The policy of National Institute of Standards and Technology (NIST) is to use metric units of measurement in all its publications, and to provide statements of uncertainty for all original measurements. In this paper however, data from organizations outside NIST are shown, which may include measurements in non-metric units or measurements with very limited uncertainty statements.

[22] was used as the ignition source. A 100 % cotton fabric, white plain weave of (19 to 33) threads/cm^2 and surface density of (115 ± 1) g m^{-2} was used as a cover sheeting.

2.2. Test configurations for reduced-scale mock-ups: standard and modified mock-ups with foam thickness of 51 mm, 76 mm and 102 mm

Six different mock-up configurations were adopted for reduced-scale testing: three "standard mock-ups" (SMs) with a foam thickness of 51 mm, 76 mm or 102 mm, and three "modified mock-ups" (MMs) with a foam thickness of either 51 mm, 76 mm or 102 mm. In the SMs, the foam was in direct contact with the wooden frame, whereas, in the MMs, the foam was in contact with a metal wire mesh spaced 12.5 mm from the wood frame (see Fig. 1). In the remainder of the paper, SM2 will refer to the standard mock-up with a 51 mm-thick foam, SM3 to the standard mock-up with a 76 mm-thick foam, and SM4 to the standard mock-up with a 102 mm-thick foam; similarly, MM2 will refer to the modified mock-up with a 51 mm-thick foam, MM3 to the modified mock-up with a 76 mm-thick foam, and MM4 to the modified mock-up with a 102 mm-thick foam. Test configurations SM4 and MM4 were only simulated.

A detailed description of these test configurations was previously reported for 76 mm-thick foams [3,16] (see Fig. 1). Briefly, two pieces of FPUFs are placed, one vertically and one horizontally, at right angles to one another, simulating the crevice formed by the seat and back of a RUF. The two pieces of FPUFs were covered with upholstery fabric. The cigarette ignition source was placed along the crevice formed by the two pieces of FPUFs and it was covered by a standard sheeting (UF-400 type; Test Fabrics Inc.). In SM2 and MM2, foam dimensions were 203 mm × 203 mm × 51 mm for the vertical foam panel and 203 mm × 127 mm × 51 mm for the horizontal foam panel. In SM3 and MM3, foam dimensions were 203 mm × 203 mm × 76 mm for the vertical foam panel and 203 mm × 127 mm × 76 mm for the horizontal foam panel. In SM4 and MM4, foam dimensions were 203 mm × 203 mm × 102 mm for the vertical foam panel and 203 mm × 127 mm × 102 mm for the horizontal foam panel. The dimensions of the cover fabrics were reduced in the modified mock-ups as compared to the standard mock-ups so that the wire-mesh was in direct contact with the wire mesh (see Fig. 1). This was intended to promote oxygen supply to the smoldering front in the modified mock-ups. The dimensions of the cover fabric were as follows: (305 mm × 203 mm) for the horizontal foam panel and (457 mm × 203 mm) for the vertical foam panel in SM2; (330 mm × 203 mm) for the horizontal foam panel and (508 mm × 203 mm) for the vertical foam panel in SM3; (178 mm × 203 mm) for the horizontal foam panel and (203 mm × 203 mm) for the vertical foam panel in MM2; (203 mm × 203 mm) for the horizontal foam panel and (203 mm × 203 mm) for the vertical foam in MM3 panel.

Noticeably, SM2 is the test configuration specified in US standard test methods (*e.g.*, UFAC [6], ASTM E1353 [7], NFPA 260 [8]) and the only RUF statutory standard (TB117-2013 [9]).

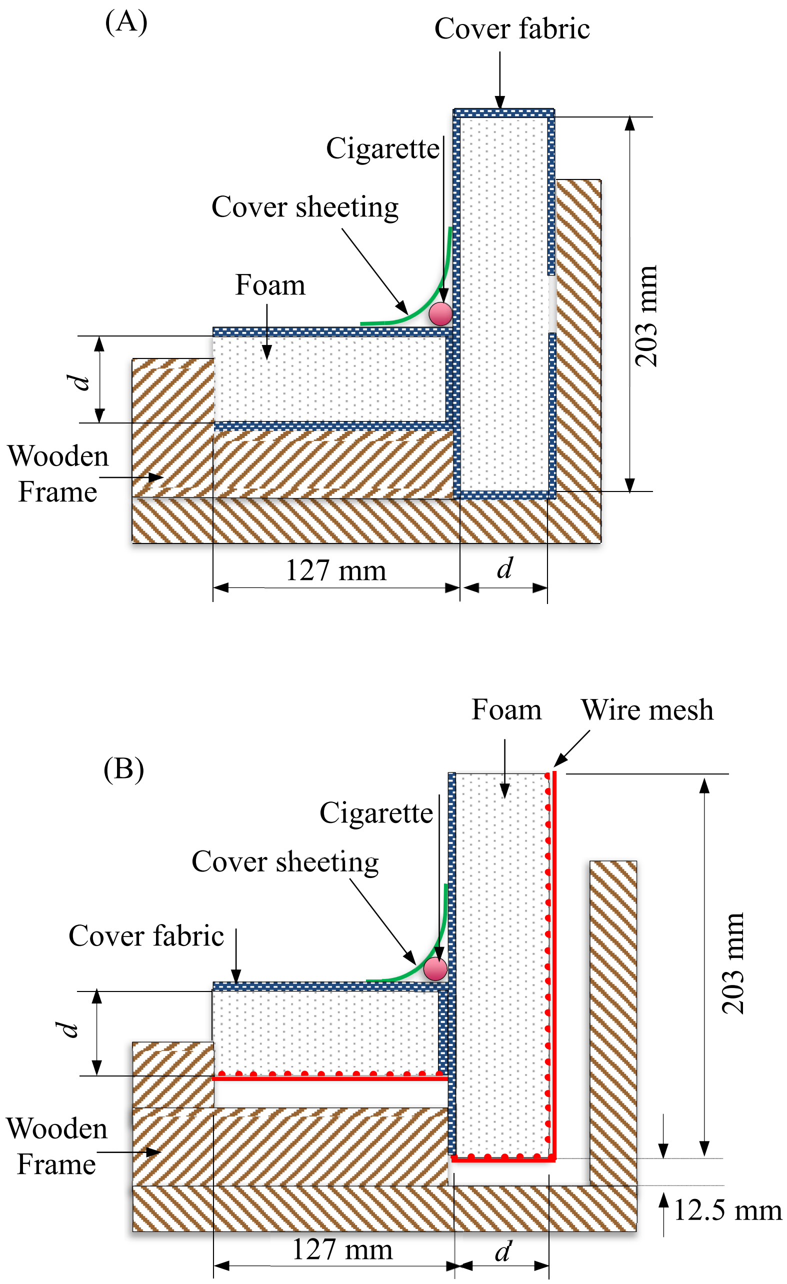

Fig. 1. Schematic drawings (side view, not to scale) of: (A) standard mock-ups (SMs) (mock-ups are in direct contact with the wooden frame), and; (B) modified mock-up (MMs) (a wire mesh separates the mock-up from the wooden frame). The foam thickness *d* was 51 mm, 76 mm or 102 mm.

2.3. Test procedure

The test procedure was based on TB-117-2013 [9]. Briefly, a lit cigarette was placed in the crevice formed by the two pieces of FPUFs and was then covered by the cover sheeting. The test duration was 45 min for SMs and 35 min for MMs. The mass loss of the mock-up (equals to the sum of the mass losses of the foam, fabrics, cotton sheeting and cigarette) was recorded in real-time.

3. Computational model

3.1. Model assumptions and model geometry

Due to the complexity of the smoldering problem, the following assumptions had to be adopted in the model:
(1) the thermal properties of FPUF are temperature-independent;
(2) gas-phase reactions are neglected;
(3) boundary layer flows are neglected;
(4) a constant heat flux from the cigarette to the FPUF is assumed;
(5) FPUF volume shrinkage is negligible;
(6) effects of fabric and cotton sheeting are not simulated.

The geometries adopted in the 2-D computational model for the mock-ups with 51 mm-thick, 76 mm-thick and 102 mm-thick foams are shown in Fig. 2. Here, the smoldering propensities of mock-ups with 102 mm-thick foams are also simulated to investigate the effect of the wire mesh on smoldering with a foam thickness that more closely resembles the one usually adopted in RUF.

The heating boundary BC, representing the location where the heat transfer between the cigarette and the foam occurs, is a quarter-circle arc with a nominal radius (r) of 10 mm. The actual radius of the cigarette was about 4 mm, however the radius r was increased to 10 mm to account for the thickness of the cover fabric and the fact that the actual heating boundary expands over time due to smoldering of the cover fabric in experiments. The center of the arc (o) was used as the origin of the coordinate system (see Fig. 2).

(A) 51 mm-thick foam

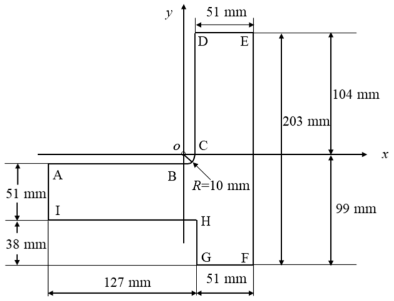

(B) 76 mm-thick foam

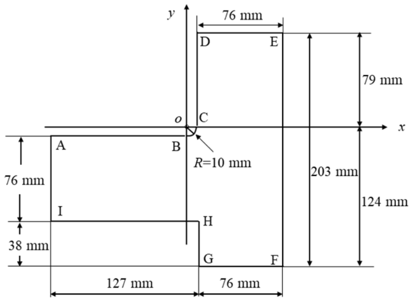

(C) 102 mm-thick foam

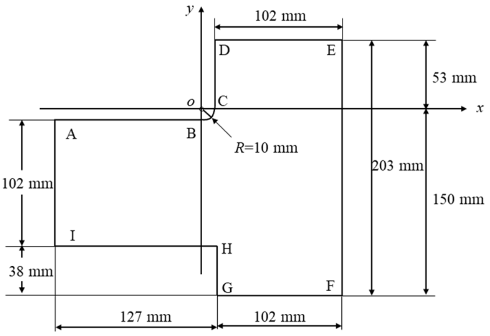

Fig. 2. Geometry of computational domain for: (A) 51 mm-thick foam; (B) 76 mm-thick foam, and; (C) 102 mm-thick foam.

3.2. Two-dimensional governing equations

The three-step reaction scheme developed by Leach *et al.* [17] was applied in this computational model. This reaction scheme with simplified kinetics was widely used and validated for both smoldering ignition and smoldering propagation [17-18]. Non-thermal equilibrium between the solid and gas phases was considered. The reaction scheme, including foam pyrolysis (*fp*), foam oxidation (*fo*), and char oxidation (*co*), is expressed as follows:

$$\text{Foam} \rightarrow v_{c,fp}\text{Char} + v_{g,fp}\text{Gas} \tag{\textit{fp}}$$

$$\text{Foam} + v_{O_2,fo}\text{O}_2 \rightarrow v_{c,fo}\text{Char} + v_{g,fo}\text{Gas} \tag{\textit{fo}}$$

$$\text{Char} + v_{O_2,co}\text{O}_2 \rightarrow v_{a,co}\text{Ash} + v_{g,co}\text{Gas} \tag{\textit{co}}$$

Non-dimensional reaction rates are expressed by the Arrhenius law,

$$\dot{\omega}_k''' = A_k e^{-\frac{E_k}{RT}}(y_{k,A})^{n_k}(y_{O_2})^{n_{O_2,k}}, \tag{1}$$

where A_k and E_k are the pre-exponential factor (s^{-1}) and the activation energy (kJ mol^{-1}) for reaction k, respectively; $(y_{k,A})^{n_k}$ and $(y_{O_2})^{n_{O_2,k}}$ are the reaction modes for reactant A in each chemical reaction and oxygen, respectively; $y_{k,A}$ and y_{O_2} are the mass fraction of solid-phase species A and oxygen, respectively, which are normalized by the initial total mass; n_k, $n_{O_2,k}$ are the reaction orders.

The conservation equations are: Eq. (2) solid-phase mass, Eqs. (3-5) solid-phase species mass, Eq. (6) solid-phase energy, Eq. (7) gas-phase energy, Eq. (8) gas-phase mass, Eq. (9) gas-phase species mass, Eq (10). gas momentum of porous flow (Brinkman equation). The gas state equation is expressed by Eq. (11).

$$\frac{\partial \bar{\rho}}{\partial t} = -\bar{\rho}|_{t=0}\dot{\omega}_{fg}''' \tag{2}$$

$$\frac{\partial y_f}{\partial t} = -\dot{\omega}_{fp}''' - \dot{\omega}_{fo}''' \tag{3}$$

$$\frac{\partial y_c}{\partial t} = v_{c,fp}\dot{\omega}_{fp}''' + v_{c,fo}\dot{\omega}_{fo}''' - \dot{\omega}_{co}''' \tag{4}$$

$$\frac{\partial y_a}{\partial t} = v_{a,co}\dot{\omega}_{co}''' \tag{5}$$

$$(\rho c)_{s,eff}\frac{\partial T_s}{\partial t} = \nabla \cdot (k_{s,eff}\nabla T_s) + \textstyle\sum_k \bar{\rho}|_{t=0}\,\dot{\omega}_k''' \Delta H_k + h_{sg}(T_g - T_s) \tag{6}$$

$$(\varphi \rho_g c_g)\frac{\partial T_g}{\partial t} + \rho_g c_g \boldsymbol{u} \cdot \nabla T_g = \nabla \cdot (\varphi k_g \nabla T_g) + h_{sg}(T_s - T_g) \tag{7}$$

$$\frac{\partial(\varphi\rho_g)}{\partial t} + \nabla \cdot (\rho_g \boldsymbol{u}) = \bar{\rho}|_{t=0}\dot{\omega}'''_{fg} \tag{8}$$

$$\rho_g \frac{\partial y_j}{\partial t} + \rho_g(\boldsymbol{u} \cdot \nabla)y_j = \nabla(\rho_g D \nabla y_j) + \bar{\rho}|_{t=0}(\dot{\omega}'''_{f,j} - \dot{\omega}'''_{d,j}) \tag{9}$$

$$\frac{\rho_g}{\varphi}\left(\frac{\partial \boldsymbol{u}}{\partial t} + (\boldsymbol{u} \cdot \nabla)\frac{\boldsymbol{u}}{\varphi}\right) = \nabla \cdot \left[-p\boldsymbol{I} + \frac{\mu}{\varphi}(\nabla\boldsymbol{u} + (\nabla\boldsymbol{u})^T - \frac{2\mu}{3\varphi}(\nabla \cdot \boldsymbol{u})\boldsymbol{I}\right] -$$

$$\left(\frac{\mu}{K} + \frac{\bar{\rho}|_{t=0}\dot{\omega}'''_{fg}}{\varphi^2}\right)\boldsymbol{u} + \rho_g \boldsymbol{g} \tag{10}$$

$$p = \frac{\rho_g}{M_{mix}} R T_g, M_{mix} = 1/(\textstyle\sum_j y_j/M_j) \tag{11}$$

Porous flow is described by extending Darcy's law to consider the dissipation of the kinetic energy by viscous shear [23]. The mass fraction of solid-phase species (y_i) and gas-phase species (y_j), are normalized by the initial total mass. Subscripts *f*, *c*, *a* represent foam, char, and ash, respectively. The subscript "*j*" represents gas-phase species, including oxygen (O_2), nitrogen (N_2) and gas products (gp). The effective volumetric heat capacity and thermal conductivity in Eq. (6) incorporate linear property variation with foam components, *i.e.* $c_{s,eff} = \sum_i y_{s,i} c_{s,i}$ and $k_{s,eff} = \sum_i X_{s,i} k_{s,i}$. Here X denotes the volume fraction, deduced from the mass fraction $X_{s,i} = \rho_{b,0}\, y_{s,i} / \rho_{b,i}$. The definition of other symbols can be found in the Nomenclature. Here, optimized kinetic parameters for FPUF obtained from genetic algorithms [18] are used (see Table 1). Values of major physical parameters used in the model are listed in Table 2.

Table 1. Chemical kinetic parameters from [18]

Parameters/*k*	***fp***	***fo***	***co***
A_k (s^{-1})	5×10^{15}	2×10^{12}	4×10^{13}
E_k (kJ mol^{-1})	200	155	185
n_k (-)	3	1	1
$n_{O2,k}$	0	1	1
$v_{s,k}$ (-)	0.05	0.4	0.3
ΔH_k (J g^{-1})	775	-900	-4600
$v_{O2,k}$ (-)	0	0.12	0.62

Table 2. Physical parameters used in the computational model

Parameter	Value	Reference sources
k (W m^{-1} K^{-1})	$k_f = 0.063$	[17]
	$k_c = 0.042$	
	$k_a = 0.03$	
	$k_g = 0.0258$	
c (J kg^{-1} K^{-1})	$c_f = 1700$	[24]
	$c_c = c_\alpha = 1260$	
	$c_g = 1100$	
ρ_0 (kg m^{-3})	$\rho_{f,0} = 26.5$	this work
	$\rho_{c,0} = \rho_{f,0} \times \nu_{c,fo},$	
	$\rho_{a,0} = \rho_{c,0} \times \nu_{a,co}$	
	$\rho_{g,0} = 1.178$	
d_p (mm)	$d_p = 0.5$	[19]
ρ_s (kg m^{-3})	$\rho_{s,f} = 1034$	deduced by $\rho_s = \rho_0/(1-\varphi_0)$
	$\rho_{s,c} = \rho_{s,a} = 500$	
φ_0 (-)	$\varphi_{f,0} = 0.974$	[17, 25]
	$\varphi_{c,0} = \varphi_{a,0} = 0.98$	
μ (kg m^{-1} s^{-1})	$\mu = 2.50\times10^{-5}$	[25]
D (m^2 s^{-1})	$D = 4.53\times10^{-5}$	[25]
K (m^2)	$K_f = 2.76\times10^{-9}$	[25]
	$K_c = K_a = 8.4\times10^{-7}$	
h_c (W m^{-2} K^{-1})	$h_c = 8$	estimated by $h_c = 1.87\times(T_s-T_0)^{0.25}$ [26]
h_m (kg m^{-2} s^{-1})	$h_m = 0.006$	deduced by $h_m = h_c/(\rho_g c_g Le^{2/3})$ [17]
h_{sg} (W m^{-3} K^{-1})	$h_{sg} = 4.5\times10^6$	estimated by $Nu = 2+1.1Re^{0.6}Pr^{1/3} = (h_{sg}\times d_f)/k_g$ [17]

3.3. Boundary and initial conditions

The boundary conditions for solid-phase energy (Eq. (6)), gas-phase species mass (Eq. (9)) and momentum conservation of porous flow (Eq. (10)) are listed in Table 3, Table 4 and Table 5, respectively. In Table 3, the thermal boundary condition imposed on AB, BC, CD, DE in SM is the same as those in MM. A constant heat flux $\dot{q}''_{\mathrm{ig}}$ of 2.5 kW · m^{-2} for 10 min is imposed on the arc boundary BC to trigger the smoldering ignition. The total energy input (1.5 MJ · m^{-2}) is comparable to the energy input selected by Ohlemiller *et al.* [15] (1.88 MJ · m^{-2} - 2.3 MJ · m^{-2} with a heat flux of 6.3 kW · m^{-2} to 8.4 kW · m^{-2} for 5 min). The heat flux $\dot{q}''_{\mathrm{ig}}$ and heating time t_{ig} are such that the maximum temperature at BC is never greater than 900 °C (the maximum temperature at the periphery of the cigarette tobacco coal [27, 28]).

At boundaries of EF, FG, GH, HI, IA, the adiabatic condition is used for SM while the convective cooling boundary condition is applied for MM. In Table 4, only AB, BC, CD, DE boundaries are permeable to air/gas of pyrolysis in SM, while all the boundaries are permeable in MM. In Table 5, the open boundary condition is applied on the AB, BC, CD, DE in SM, which is used on all the boundaries in MM. When combined with the following initial conditions (Eq. (12), the system of equations is closed.

$$\begin{aligned} &y_{f,0} = 1,\ y_{c,0} = y_{a,0} = 0,\ y_{O_2,0} = 0.23,\ y_{N_2,0} = 0.77,\ y_{gp,0} = 0 \\ &T_{s,0} = T_{g,0} = 293\ \mathrm{K},\ \mathbf{u}_0 = 0, p_0 = 1.013\times10^5\ \mathrm{Pa} \end{aligned} \quad (12)$$

Eqs. (1) - (11) are highly nonlinear and are discretized over non-uniform elements. The equations are solved using the fully - coupled solver in COMSOL Multiphysics by the finite element method. The domain is meshed into free triangles and simulations are performed with an initial time step of 0.01 s and a maximum time step of 1 s. The element size varies between a minimum of 0.05 mm and a maximum of 3 mm, and the number of domain elements in a complete mesh ranges between 8048 and 13107. The relative difference between two adjacent iteration values (relative tolerance) is set to less than 10^{-3}. If this criterion is not met after 100 iterations, the time step is halved, and the cycle repeated. The calculation is completed when all relative tolerances are less than 10^{-3}. A mesh/time step independence study for SM3 showed that refining the mesh by doubling the number of triangles and reducing the maximum time step by a factor of 4 resulted in a 7-fold increase in computing time, but had a minor effect on simulated smoldering temperature (less than 2.5 % variation in the peak smoldering temperature at $t = 15$ min). Thus, the equation system was sufficiently resolved. A sensitivity analysis was performed (see Fig. A1 in the Appendix) to identify the most important model inputs for the simulated results.

Table 3. Boundary conditions for the solid-phase energy equation (Eq. (6))

Configuration	Boundary	Boundary conditions
SM	BC	$-\mathbf{n}\cdot k_s\nabla T_s = q''_{ig} - h_c(T_s - T_\infty) - \varepsilon\sigma(T_s^4 - T_\infty^4)$
	AB, CD, DE	$-\mathbf{n}\cdot k_s\nabla T_s = -h_c(T_s - T_\infty)$
	EF, FG, GH, HI, IA	$-\mathbf{n}\cdot k_s\nabla T_s = 0$
MM	BC	$-\mathbf{n}\cdot k_s\nabla T_s = q''_{ig} - h_c(T_s - T_\infty) - \varepsilon\sigma(T_s^4 - T_\infty^4)$
	Other boundaries	$-\mathbf{n}\cdot k_s\nabla T_s = -h_c(T_s - T_\infty)$

Table 4. Boundary conditions for the gas-phase species mass equation (Eq. (9))

Configuration	Boundary	Boundary conditions
SM	AB, BC, CD, DE	$-\mathbf{n}\cdot\rho_g D\nabla y_{g,j} = -h_m(y_{g,j} - y_\infty)$
	EF, FG, GH, HI, IA	$-\mathbf{n}\cdot\rho_g D\nabla y_{g,j} = 0$
MM	All boundaries	$-\mathbf{n}\cdot\rho_g D\nabla y_{g,j} = -h_m(y_{g,j} - y_\infty)$

Table 5. Boundary conditions for the Brinkman equation (Eq. (10))

Configuration	Boundary	Boundary conditions
SM	AB, BC, CD, DE	$p = p_0$
	EF, FG, GH, HI, IA	$-\mathbf{n}\cdot\rho_g\mathbf{u} = 0$
MM	All boundaries	$p = p_0$

4. Experimental results and discussion

For each test configuration of SM2, SM3, MM2 and MM3, the mass loss of the mock-up (sum of the mass losses of the foam, fabrics, cotton sheeting and cigarette) was measured. The average mass loss *vs.* time (solid line) and the standard deviation *vs.* time (shaded area), calculated over three replicate tests for each of the mock-up configurations, are plotted in Fig. 3.

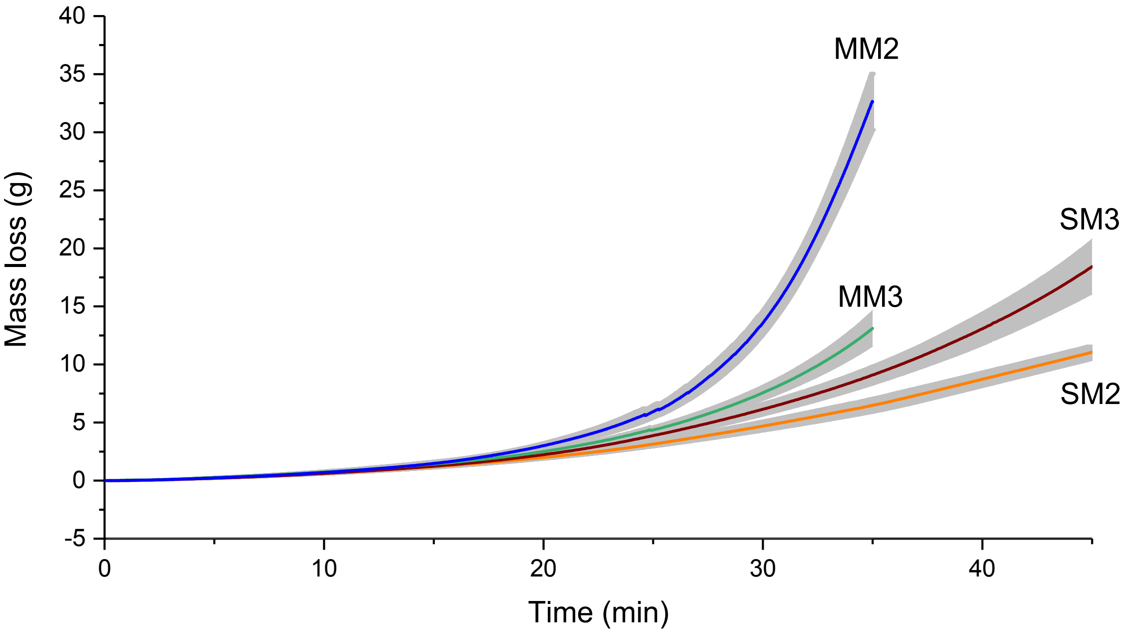

Fig. 3. Average mass loss data (solid line) and standard deviation (shaded area) for three replicate tests measured in SM2, SM3, MM2 and MM3.

The test duration was 45 min for SM and 35 min for MM. As shown in Fig. 3, the effect of the test configuration was remarkable. At $t = 35$ min, the values of mass loss were 6.5 ± 0.6 g, 9.1 ± 0.9 g, 13.1 ± 1.6 g, and 32.6 ± 2.4 g for SM2, SM3, MM3 and MM2, respectively. The mass loss at $t = 35$ min showed an approximate 0.5-fold increase in modified mock-up as compared to the standard mock-up with a foam thickness of 76 mm (compare MM3 and SM3 in Fig. 3), and a 4-fold increase with a foam thickness of 51 mm (compare MM2 and SM2 in Fig. 3). These data not only confirm the previously published work indicating that the mock-up mass loss measured in MM is significantly higher than the one measured in SM [16], but also identify the importance of foam thickness on the mass loss. Based on these data, the effect of the mock-up type (*i.e.*, SM *vs.* MM) increased roughly by one order of magnitude when the foam thickness was reduced from 76 mm to 51 mm.

For the SM, the thinner the foam is the closer the smoldering front is to the wooden frame and, as a result, a more severe suppression of the airflow is expected at the bottom of the mock-up (see Sec. 5.1). For the MM, the thinner the foam is the lower is the resistance (*i.e.*, pressure drop) to the buoyant airflow through the bottom of the mock-up is expected to be (see Sec. 5.2). These results have important implications on the choice of a proper mock-up test to predict full-scale smoldering behaviour. At foam thicknesses of 102 mm (about 4 inch) and above, typically used in RUF, the effect of the wooden substrate on buoyant airflow in the standard mock-up further decreases as compared to SM3 and the effect of pressure drop in the modified mock-up further increases as compared to MM3; thus, the ranking of smoldering propensity by mass loss is expected to be the following:

$$ML(t)_{SM2} < ML(t)_{SM3} < ML(t)_{SM4} < ML(t)_{MM4} < ML(t)_{MM3} < ML(t)_{MM2} \tag{13}$$

where $ML(t)_x$ is the mock-up mass loss at time t for the six combinations of two mock-up configuations and three foam thicknesses. The speculated smoldering propensity in SM4 and MM4 (Eq. (13)) will be further verified by our computational model. The inequality (13) suggests that in RUF with foam thickness above 51 mm (large majority of RUF), SM2 is expected to underestimate smoldering mass loss and MM2 is expected to overestimate smoldering mass loss. Hence, SM2 does not appear to be a robust predictor of smoldering in RUF and MM2 may offer a near-worst-case scenario, useful to identify the upholstery materials that prevent most smoldering ignitions independent of the construction and geometry of the actual furniture.

5. Modelling results and discussion

5.1. Smoldering behavior in SM

Fig. 4 shows smoldering temperature fields and airflow streamlines for SM3 at $t = 15$ min, 30 min, 45 min, and 60 min. The same ranges are used for each case. The temperature fields are displayed by rainbow maps in Fig 4A, 4C, 4E, 4G. A grayscale map is adopted for the smoldering temperature fields, and a rainbow map is used for the streamlines in Fig. 4B, 4D, 4F, 4H. The rainbow temperature map is preferred to display the magnitude of smoldering temperature, whereas the grayscale temperature map is used to visualize the impact of temperature on the airflow streamlines. The airflow arrows and colored streamlines on the velocity map in Fig. 4B, 4D, 4F, 4H indicate the directions and magnitudes of airflow, respectively.

At $t = 15$ min (Fig. 4A), the smoldering region (defined as the charred foam zone where the foam oxidation front passed through) extends from the heating boundary BC without reaching the bottom and right side of the mock-up. A peak temperature of 353 °C is achieved in the upper region ($y > 0$). Fig. 4B shows that air enters the smoldering region through boundaries AB, BC and CD, then, the airflow is mixed with gaseous pyrolyzates in the smoldering region and released to the environment through the top boundary DE.

The temperature gradient in the gas flow field gives rise to a density gradient that acts as a driving force for natural convection and generates a buoyant airflow [29]. In the bottom region of the mock-up, buoyant flow is allowed, but it does not draw air through the impermeable boundaries of EF, FG, GH, HI and IA; in the top-left region of the mock-up, a buoyant airflow is generated but the streamlines indicate that this buoyant airflow has only a marginal effect on oxygen supply to the smoldering region. Hence, oxygen supply in SM appears to be mainly driven by oxygen diffusion through boundaries AB, BC and CD at $t = 15$ min.

At $t = 30$ min (Fig. 4C), the smoldering zone has reached the impermeable boundary EF with a peak temperature of 356 °C in the upper region ($y > 0$). The upward smoldering front is gradually approaching the top free boundary DE. The gas flow is mainly driven from boundary BC and CD to the smoldering zone (Fig. 4D).

At t = 45 min (Fig. 4E), the peak smoldering temperature increases to 488 °C in the upper region. Velocity streamlines show a reduction in magnitude as compared to t = 30 min, but the air supply is still mainly driven by airflow through boundaries AB, BC and CD (Fig. 4F).

For $t > 45$ min, the smoldering region propagates downward and, at t = 60 min (Fig. 4G), a peak temperature of 378 °C is reached in the lower region. This upward buoyant airflow does not increase oxygen supply to the downward smoldering front, which is located in the bottom right of the mock-up (see Fig. 4H). Thus, for 15 min < t < 60 min oxygen supply in SM appears to be still dominated by oxygen diffusion from boundaries AB, BC and CD to the smoldering front.

Fig. S1 in supplemental information provide additional details about the simulated smoldering temperature profiles, as well as the bulk density of the foam component, the mass fraction of oxygen, the foam pyrolysis rate, the foam oxidation rate and the char oxidation reaction rate along the mid-section of the vertical foam in SM3.

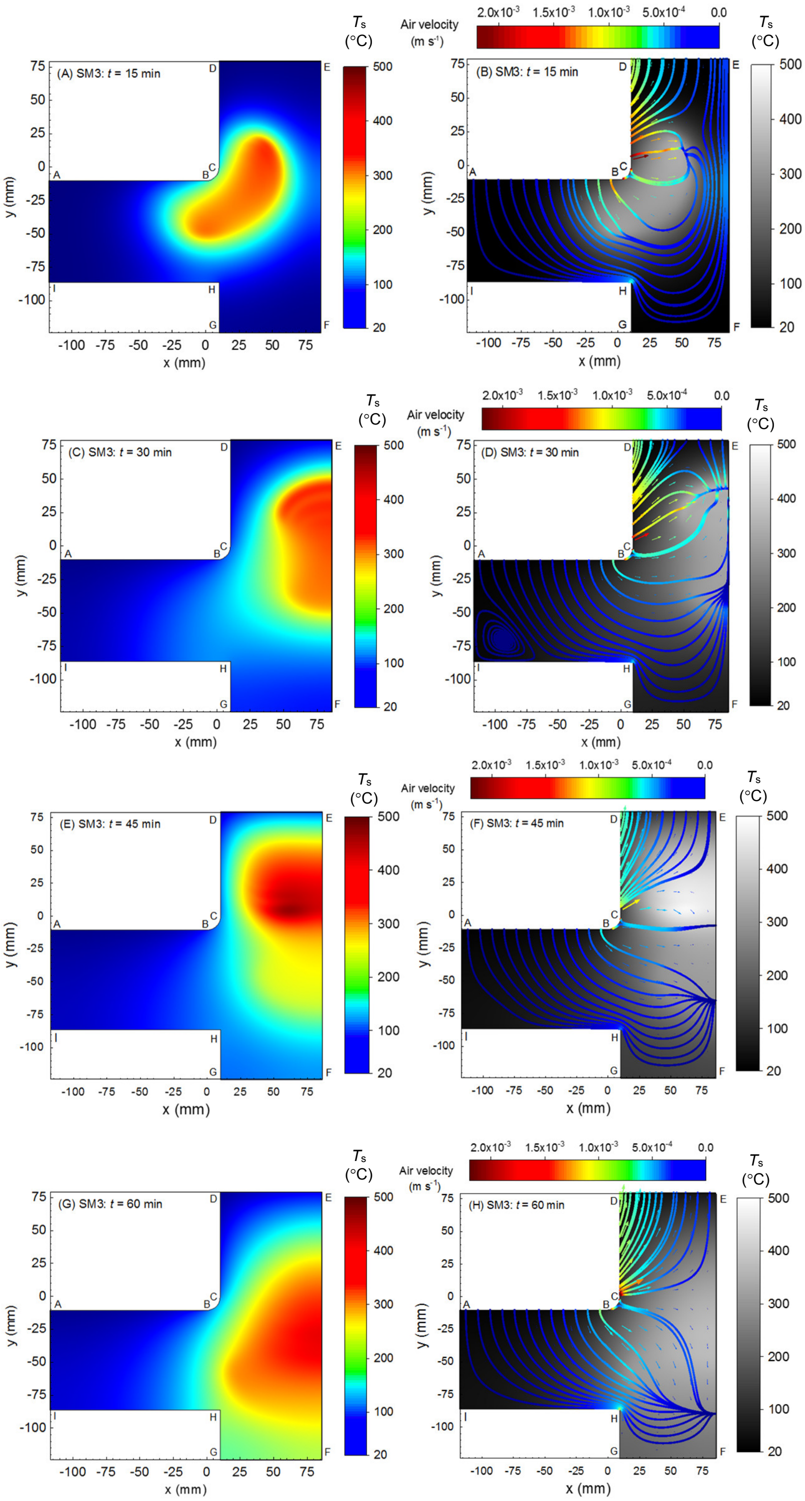

Fig. 4. Simulated smoldering temperature field (rainbow map) in SM3 at (A) t = 15 min, (C) t = 30 min, (E) t = 45 min, and (G) t = 60 min; and simulated streamlines for gas flow velocity (rainbow map) and smoldering temperature field (grayscale map) in SM3 at (B) t = 15 min, (D) t = 30 min, (F) t = 45 min and (H) and t = 60 min.

5.2. Smoldering behavior in MM

Fig. 5 shows the smoldering temperature fields and streamlines for gas velocity in MM3 at t = 15 min, 30 min, 45min, and 60 min. For comparison purposes, the same range for temperature and velocity and the same combination of rainbow and grayscale maps are used as in Fig. 4.

At t = 15 min (Fig. 5A), the peak smoldering temperature in MM3 is higher as compared to SM3 (390 °C *vs.* 353 °C). The streamlines (Fig. 5B) show the generation of buoyant flow through the bottom permeable boundaries GF, IH and, to a less extent, the side permeable boundaries CD and EF. Such buoyant flow drives air into the smoldering zone and significantly, boosts oxygen supply compared to the diffusion dominated smoldering scenario observed in SM (Fig. 4B).

At t = 30 min (Fig. 5C), the outer edge of the smoldering zone has almost reached the permeable boundaries on the bottom IH and side EF. The airflow through the boundaries IH and EF is enhanced (Fig. 5D) and, the peak temperature slightly decreases as compared to t = 15 min (383 °C *vs.* 390 °C). Compared to SM3, the peak smoldering temperature at t = 30 min is higher (383 °C *vs.* 356 °C) and there is much more smoldering propagation into the bottom region (Fig. 4C).

At t = 45 min (Fig. 5E), the peak smoldering temperature increases to 500 °C (higher than the 488 °C in SM3) as the smoldering front approaches the top boundary DE. Meanwhile, the smoldering front moves towards the left and bottom of the mock-up and a strong buoyant airflow develops through the bottom permeable boundaries IH and GF (Fig. 5F).

At t = 60 min (Fig. 5G), the horizontal smoldering front reaches the left boundary AI, and the downward smoldering front reaches the bottom boundary GF. The high temperature gradient near the bottom GF, especially at the right bottom corner, induces a strong buoyant airflow which drives oxygen to the smoldering zone (Fig. 5H).

By comparing the airflow streamlines between SM and MM at t = 30 min, t = 45 min and t = 60 min, it can be concluded that the oxygen supply is dominated by a buoyant airflow from the bottom of the mock-up in MM and a diffusion-driven oxygen transport from the boundaries in proximity of the heating source in SM.

More details about the dynamic smoldering profiles along the mid-section of the vertical foam can be found in Fig. S2 in the supplemental document.

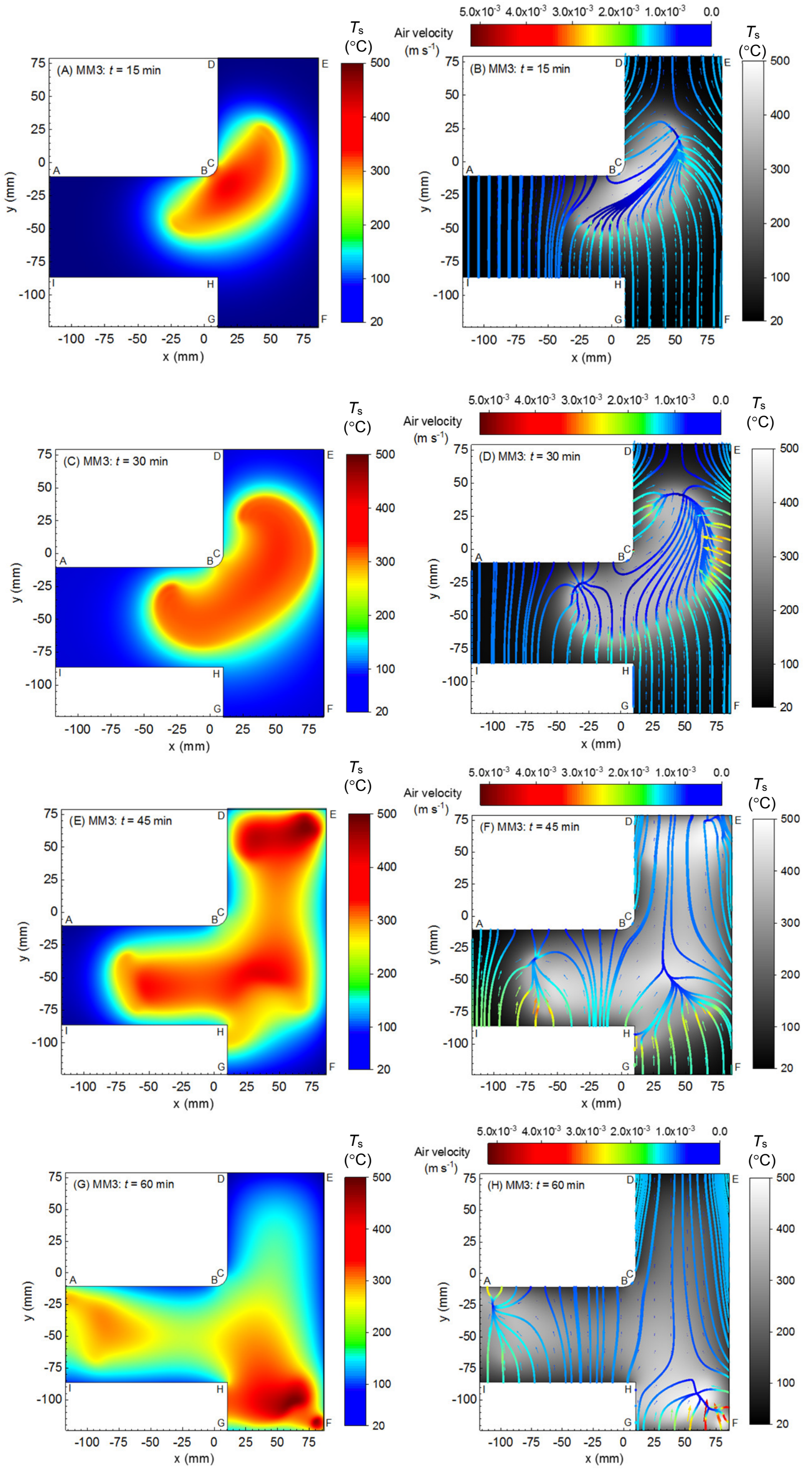

Fig. 5. Simulated smoldering temperature field (rainbow map) in MM3 at (A) t = 15 min, (C) t = 30 min, (E) t = 45 min, and (G) t = 60 min; and simulated streamlines for air velocity (rainbow map) and smoldering temperature field (grayscale map) in MM3 at (B) t = 15 min, (D) t = 30 min, (F) t = 45 min and (H) and t = 60 min.

5.3. Effects of foam thickness in SM and MM

The effects of foam thickness on smoldering in SM and MM at an early stage (t = 15 min) are shown in Fig. 6 and 7, respectively. Generally, smoldering is supported by the heat generated by foam and char oxidation. For $t \leq 15$ min, char oxidation is negligible (see supplemental material), thus, in Fig. 6 and 7 it was chosen to "visualize" the smoldering wave by displaying the foam oxidation rate in combination with air-velocity streamlines.

A rainbow map is used to display the foam oxidation rate in Fig. 6A, 6C and 6E for SM, and in Fig. 7A, 7C and 7E for MM; a gray scale map is used to display the foam oxidation rate and a rainbow map is used to display the air-velocity streamlines in Fig. 6B, 6D and 6F for SM, and Fig. 7B, 7D and 7F for MM.

In SM, the foam oxidation rates increase with foam thickness (Fig. 6A, 6C, 6E) and generate a more intense smoldering wave. A higher foam oxidation rate leads to a stronger exothermic wave, which in turn promotes a faster smoldering spread rate. Additionally, the streamlines (Fig. 6B, 6D, 6F) indicate that a stronger airflow towards the smoldering region has developed for the thicker foams, *i.e.*, relative importance of convective oxygen in-flow into the smoldering front has increased compared to diffusion. The enhanced airflow supplies more oxygen to the foam oxidation front and, thus, increases the foam oxidation rate in thicker foams. Hence, the higher the foam thickness is the higher the foam oxidation rate, the higher the oxygen consumption, and the oxygen concentration gradient are, which in turn promote oxygen diffusion to the smoldering front. These results indicate that smoldering propensity increases with foam thickness in SM.

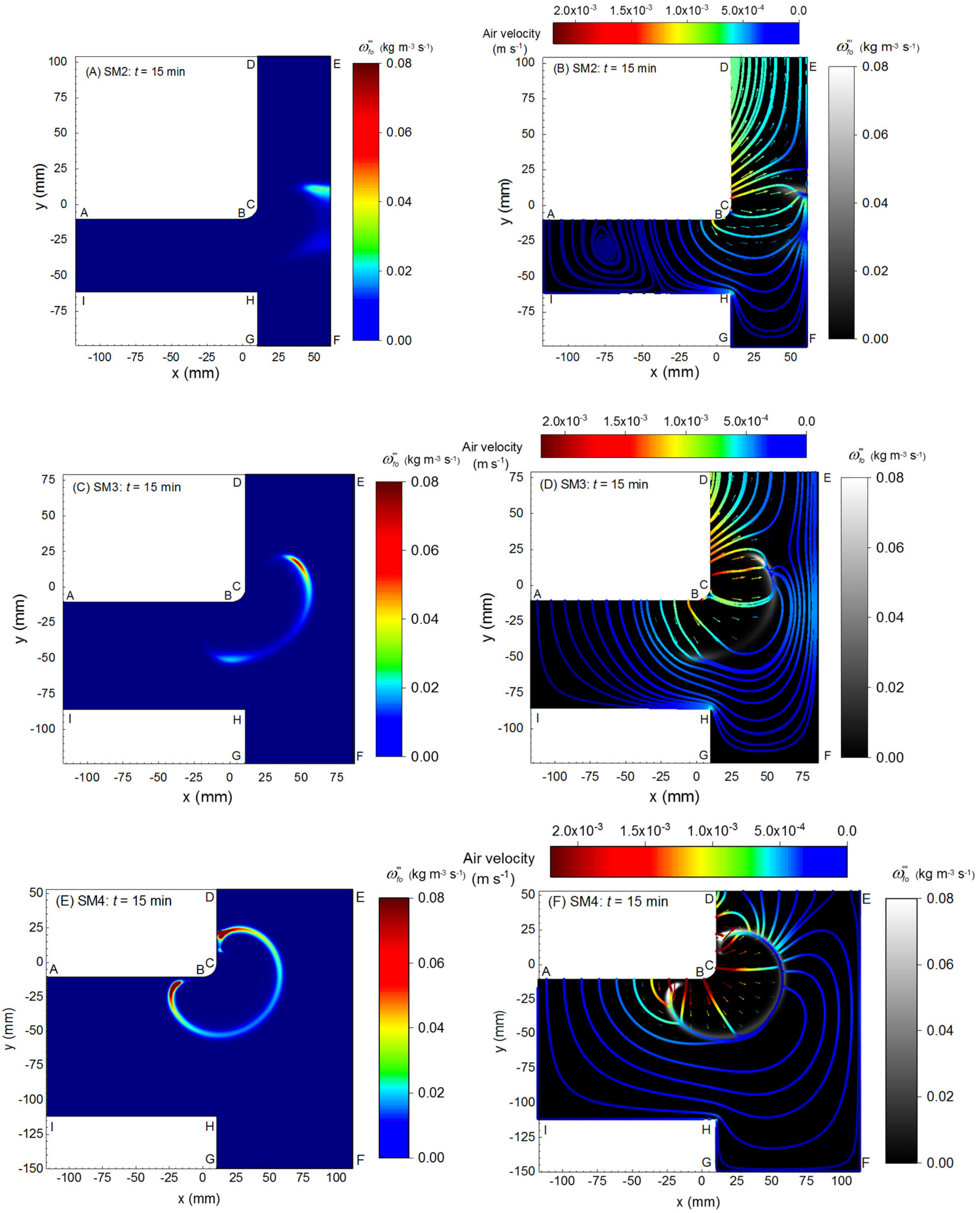

Fig. 6. Simulated foam oxidation rate (rainbow map) at t = 15 min in (A) SM2 (C) SM3, and (E) SM4; and simulated streamlines for air velocity (rainbow map) and foam oxidation rate (grayscale map) at t = 15 min in (B) SM2 (D) SM3, and (F) SM4.

An opposite trend is observed in MM as compared to SM: the foam oxidation rate (Fig. 7A, 7C, 7E) and air-velocity streamlines (Fig. 7B, 7D, 7F) appear to decrease with foam thickness. In thinner foams, both the foam oxidation rate and the spread rate of the foam oxidation wave are higher. As shown by the airflow streamlines (Fig. 7B) in MM2, the buoyant airflow gets stronger when smoldering approaches the bottom boundary IH and the right-side boundary EF. The enhanced buoyant airflow in thinner foam drives more oxygen to the foam oxidation front. The largest difference in smoldering propensity between standard mock-up and modified mock-up is observed at a thickness of 51 mm (compare SM2 in Fig. 6A-6B to MM2 in Fig. 7A-7B). Such a remarkable difference is explained by the obvious increase in oxygen supply in MM as compared to SM due to the generation of a buoyant airflow at the bottom and back side of the mock-up.

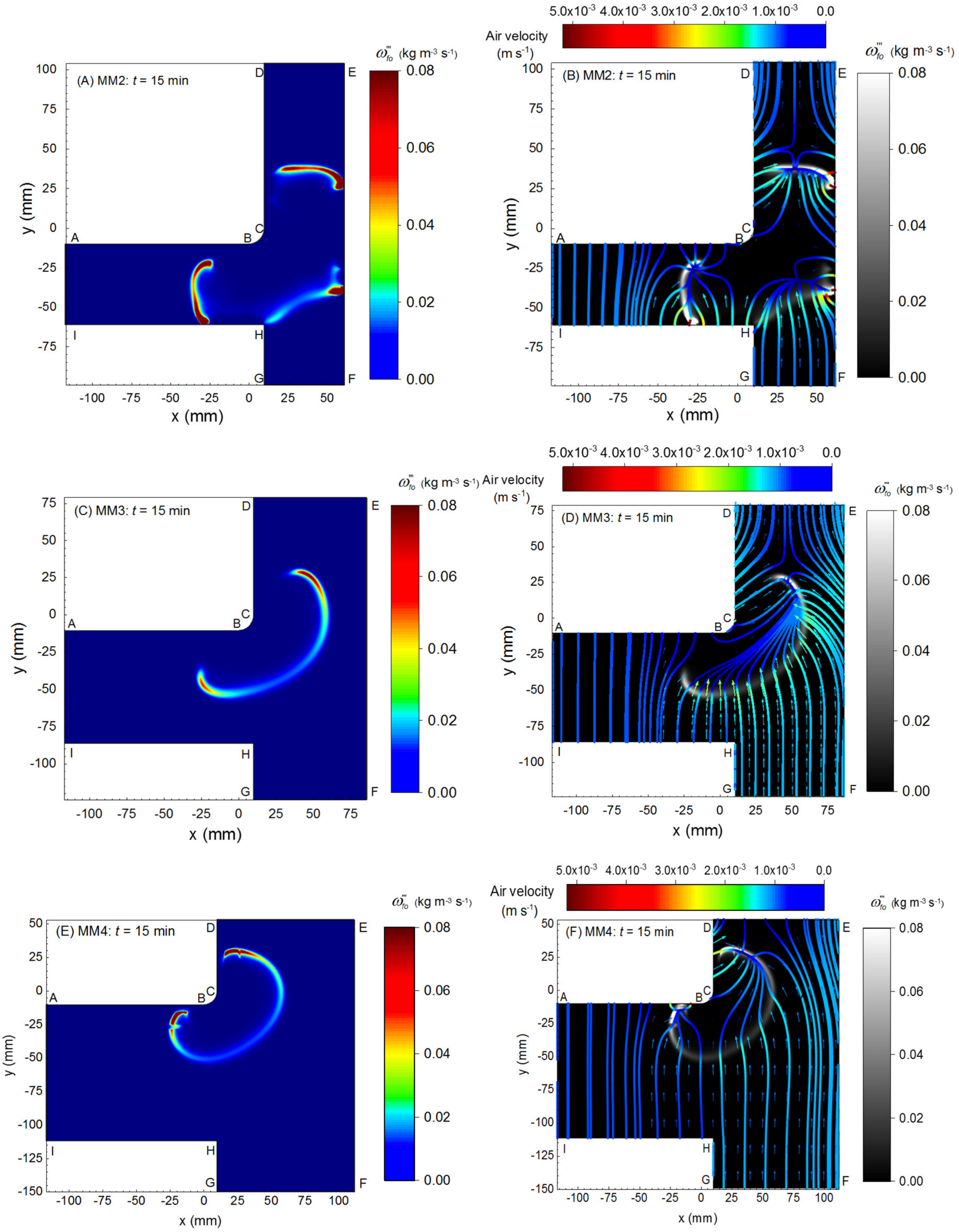

Fig. 7. Simulated foam oxidation rate (rainbow map) at t = 15 min in (A) MM2 (C) MM3, and (E) MM4; and simulated streamlines for air velocity (rainbow map) and foam oxidation rate (grayscale map) at t = 15 min in (B) MM2 (D) MM3, and (F) MM4.

A charred foam zone region, *i.e.*, where char is the major component, is formed behind the foam oxidation front. In Fig. 8, the mass fraction profiles of char at $t = 15$ min in SM and MM with foam thickness of 51 mm, 76 mm and 102 mm are displayed. By comparing the results in SM (see Fig. 8A, 8B, 8C) and MM (see Fig. 8D, 8E, 8F), it is concluded that the enhanced airflow in MM (especially in the MM2) causes a larger charred foam zone (*i.e.*, higher smoldering propensity) at $t = 15$ min. The difference between SM and MM in terms of charred-foam-zone size decreases as the foam thickness increases.

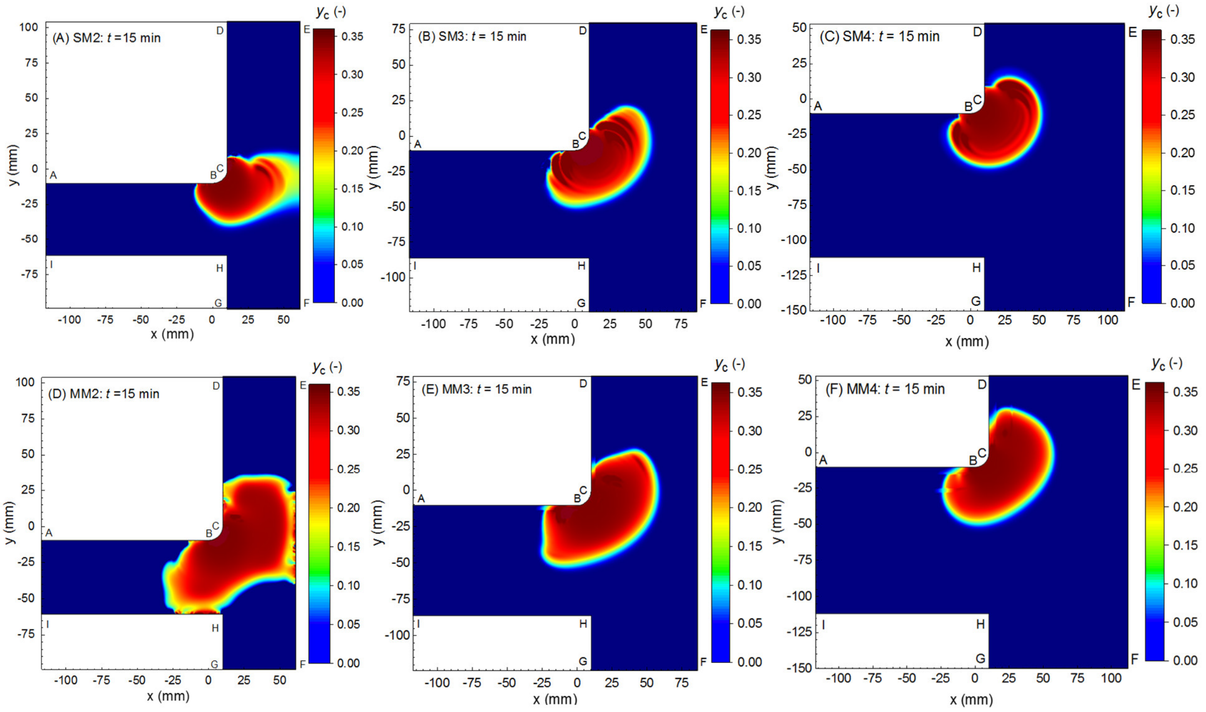

Fig. 8. Simulated mass fraction profiles of char y_c (-) at $t = 15$ min in: (A) SM2; (B) SM3; (C) SM4; (D) MM2; (E) MM3, and; (F) MM4.

5.4. Mass loss

The mass loss is a key feature that has been used to quantify smoldering propensity. In this 2-D model, the non-dimensional mass loss ($\mathrm{NML}_{2\text{-D}}$) is deduced according to Eq. (14).

$$\mathrm{NML}_{2\text{-D}} = 1 - \frac{m(t)}{m_0} = \frac{\sum_{i=1}^{N} m_{\mathrm{i},0}[1-(y_{\mathrm{i,f}} + y_{\mathrm{i,c}} + y_{\mathrm{i,a}})]}{\sum_{i=1}^{N} m_{\mathrm{i},0}} \tag{14}$$

where $y_{\mathrm{i,f}}$, $y_{\mathrm{i,c}}$, $y_{\mathrm{i,a}}$ represent the mass fraction of foam, char, and ash in mesh cell i, respectively; N is the total mesh nodes; $m_{\mathrm{i},0}$ is a constant that represents the initial mass of fuel in mesh cell *i*. The sum of initial mass fraction of solid-phase species at each mesh node is unity. The $NML_{2\text{-}D}$ indicates the mass consumption proportion over the entire 2-D computational domain.

Fig. 9 displays the comparisons of $NML_{2\text{-}D}$ for SM and MM, for foam thicknesses of 51 mm (approximately 2 inch), 76 mm (approximately 3 inch), and 102 mm (approximately 4 inch). With the increase in the foam thickness, the difference of the $NML_{2\text{-}D}$ between the SM and MM is narrowed. This means that the smoldering propensity in thinner foam is more sensitive to change of external boundary conditions. The number of mesh nodes N (the denominator in Eq. (14)) increases with the foam size. Thus, the $NML_{2\text{-}D}$ might not be a good index when comparing the mass consumption of foam with different thickness in the same mock-up. To make a better quantification of the smoldering propensity, a correlation of the mass loss (g) between the 2-D model and experiments should be developed.

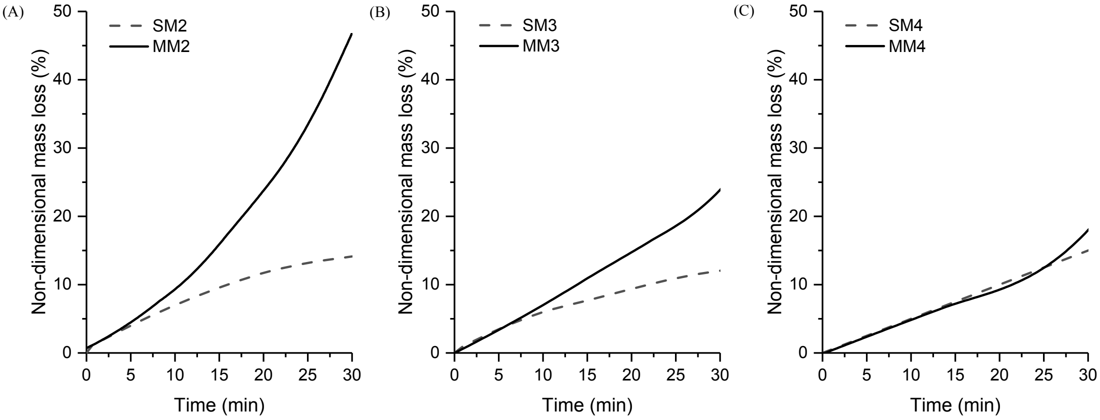

Fig. 9. Model predicted non-dimensional mass loss $NML_{2\text{-}D}$ for: (A) SM2 and MM2; (B) SM3 and MM3; and (C) SM4 and MM4.

As observed in experimental tests at $t < 30$ min, the charred foam zone behind the foam decomposition front can be approximated as a sphere of radius r with a missing semi-hemisphere (see Fig. A2 in the Appendix). Based on this approximation, the non-dimensional mass loss ($NML^*_{2\text{-}D}$) in the charred foam zone is deduced from the predicted consumed radius by the 2-D model. The radius of the charred foam zone is defined as the propagation radius of the foam oxidation front. The deduced $NML^*_{2\text{-}D}$ equals the ratio of the mass loss in the charred foam zone to the initial mass of entire foam (Eq. (15)). The equivalent radius r of the charred foam zone is a function of time, which can be deduced by the $NML_{2\text{-}D}$. It is noted that the non-dimensional mass loss $NML_{2\text{-}D}$ (Eq. (14)) in the 2-D model can also be expressed in terms of the ratio of the charred foam zone to the geometric area (see Eq. (16)). The deduced $NML^*_{2\text{-}D}$ is obtained as Eq. (17) by the combination of Eq. (15) and Eq. (16). The dimensions (w_1, w_2, h_1, h_2) of the foam is shown in Fig. 10.

$$\mathrm{NML}^*_{2\text{-D}} = \Delta m(r)/m_0 = (\rho_0 - \rho_r)\pi r^3/[\rho_0(w_1h_1l + w_2h_2l)] \tag{15}$$

$$\mathrm{NML}_{2\text{-D}} = \frac{3}{4}\pi r^2 \Big/ (w_1h_1 + w_2h_2) \tag{16}$$

$$\frac{\mathrm{NML}^*_{\text{2-D}}}{\mathrm{NML}_{\text{2-D}}} = \frac{4(\rho_0 - \rho_r)r}{3\rho_0 l} \tag{17}$$

By combining Eqs. (16) - (17), the deduced $\mathrm{NML}^*_{\text{2-D}}$ is a function of $\mathrm{NML}_{\text{2-D}}$

$$\mathrm{NML}^*_{\text{2-D}} = \frac{8(\rho_0 - \rho_r)}{3\rho_0 l}\sqrt{\frac{w_1 h_1 + w_2 h_2}{3\pi}}(\mathrm{NML}_{\text{2-D}})^{\frac{3}{2}} \tag{18}$$

Then the deduced mass loss (g) can be calculated as Eq. (19).

$$\begin{aligned}\mathrm{ML}^*_{\text{2-D}}(\mathrm{g}) &= 1000\cdot\frac{8(\rho_0 - \rho_r)}{3\rho_0 l}\sqrt{\frac{w_1 h_1 + w_2 h_2}{3\pi}}(\mathrm{NML}_{\text{2-D}})^{\frac{3}{2}} m_0 \\ &= 1000\cdot\frac{8(\rho_0 - \rho_r)}{3\sqrt{3\pi}}(\mathrm{NML}_{\text{2-D}})^{\frac{3}{2}}(w_1 h_1 + w_2 h_2)^{\frac{3}{2}}\end{aligned} \tag{19}$$

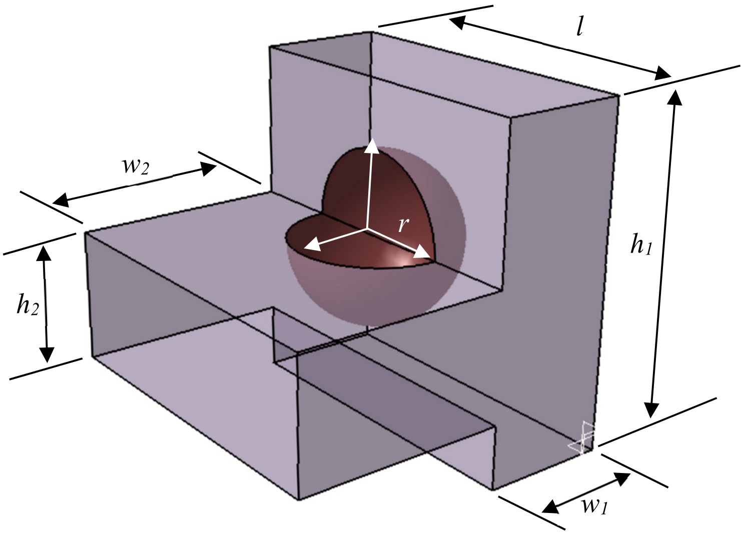

Fig. 10. Three-dimensional schematic used to calculate an approximate volume of the charred foam zone (dark color) within the virgin foam (light color).

The calculation in Eq. (19) is a rough approximation that is only valid in the early stage of tests. In fact, the charred foam zone will no longer exhibit a sphere-like geometry once the smoldering front approaches the boundaries.

Fig. 11 displays the deduced mass loss (g) in the SM and MM with foam thickness of 51 mm (SM2 and MM2), 76 mm (SM3 and MM3) and 102 mm (SM4 and MM4). At a given thickness, the MM shows a higher mass loss than the SM and this difference decreases in thicker foams. At t = 30 min, the predicted increase in mass loss is about 6-fold between SM2 and MM2, about 3-fold between SM3 and MM3, and about 1.6-fold between SM4 and MM4.

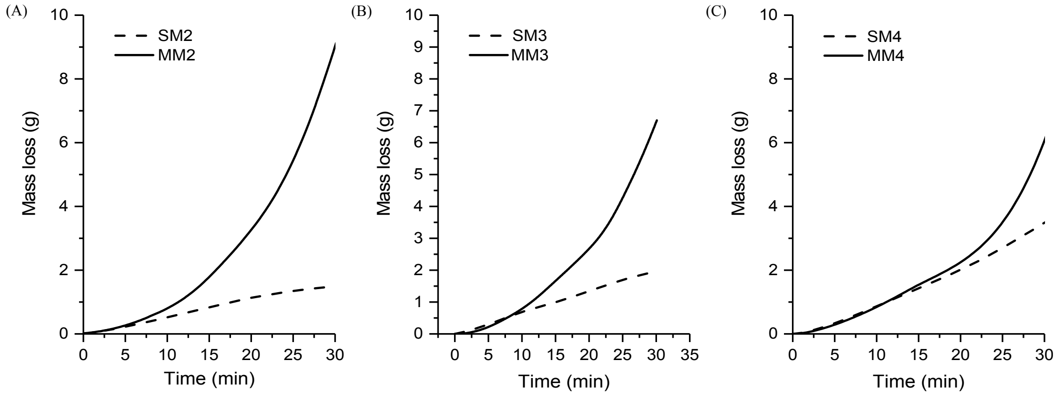

Fig. 11. Deduced mass loss by Eq. (19) for: (A) SM2 and MM2; (B) SM3 and MM3; and, (C) SM4 and MM4.

In Fig. 12 (A), the deduced mass loss curves indicate the ranking of smoldering propensity is: $ML(t)_{SM2} < ML(t)_{SM3} < ML(t)_{SM4} < ML(t)_{MM4} < ML(t)_{MM3} < ML(t)_{MM2}$. This result validates the speculation in Eq. (13) discussed in the Section 4. Fig. 12 (B) compares the deduced mass loss to the experimental mass losses in the SM2, MM2, SM3 and MM3. With an increase in foam thickness, the smoldering propensity is weakened in MM but enhanced in SM.

The model predicts the smoldering propensity ranking ($ML(t)_{SM2} < ML(t)_{SM3} < ML(t)_{MM3} < ML(t)_{MM2}$) and provides strong support for the hypothesis that the differences in smoldering behavior and propensity observed in these tests' configurations are mainly due to airflow differences.

The model underestimates the mass loss that was measured experimentally; the difference between numerical and experimental data (attributed to the assumptions applied in the model and uncertainties caused by the kinetic and physical parameters) is not considered an issue for this study because, here, the main objective of the model is to deduce the trend of smoldering propensity between different mockup configurations rather than precisely predicting the smoldering mass loss.

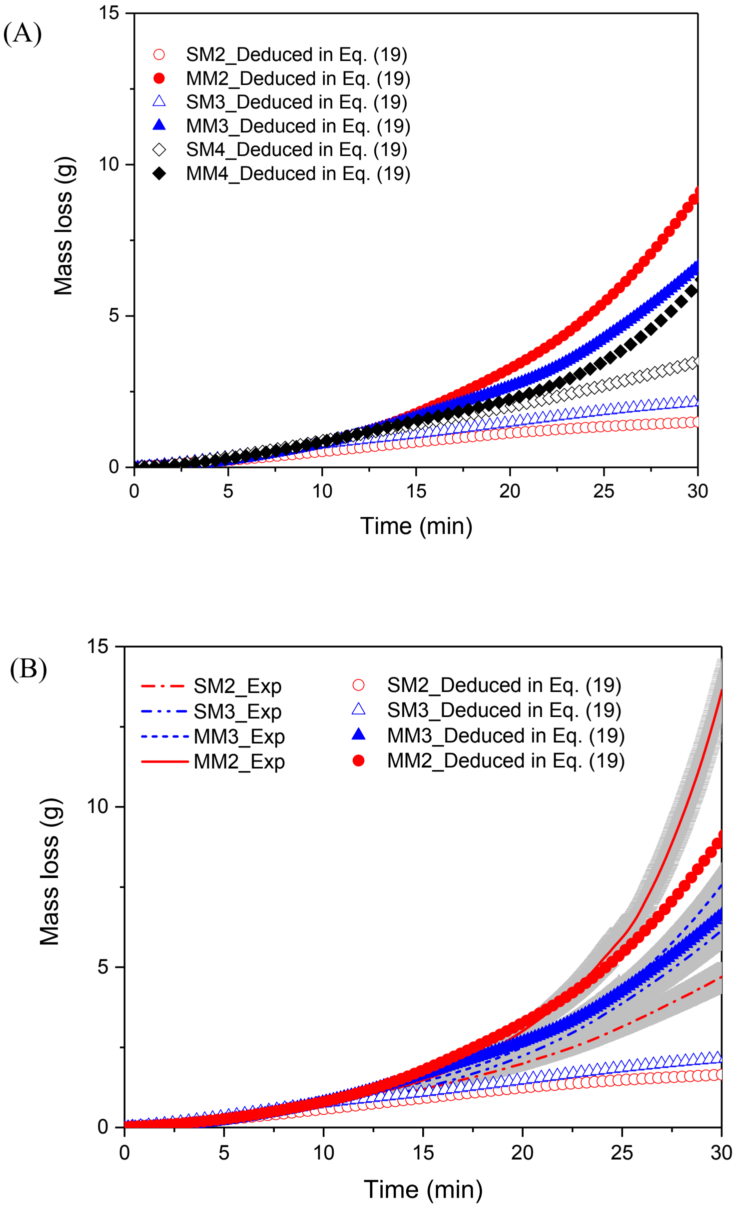

Fig. 12. (A) Deduced mass loss in SM2, SM3, SM4 and MM4, MM3, MM2, and (B) deduced mass loss *vs*. experimental mass loss in SM2, SM3 and MM3, MM2.

6. Conclusions

The smoldering behavior in the standard mock-up and modified mock-up was investigated experimentally and numerically. Experimentally, an approximate 0.5-fold increase in mass loss at t = 35 min was measured between the standard and modified mock-up with a foam thickness of 76 mm (3 inch), and a 4-fold increase was measured with a foam thickness of 51 mm (2 inch). The highest smoldering propensity was measured in the modified mock-up with a 51 mm-thick foam, and the lowest smoldering propensity was measured in the standard mock-up with a 51 mm-thick foam. At any testing time, the ranking of smoldering propensity by mass loss was $ML_{SM2} < ML_{SM3} < ML_{MM3} < ML_{MM2}$ where ML_{SM2} is the mass loss (ML) with a 51 mm-thick foam in SM, ML_{SM3} is the ML with a 76 mm-thick foam in SM, ML_{MM3} is the ML with a 76 mm-thick foam in MM and ML_{MM2} is the ML with a 51 mm-thick foam in MM.

The model indicated that oxygen supply to the smoldering front was mainly due to a buoyant airflow from the bottom of the mock-up in the MM, and a diffusion-driven oxygen transport from the boundaries in proximity of the heating source in the SM. The enhanced airflow in the MM provided more O_2 to the foam oxidation front, hence, a more intense foam oxidation, higher peak smoldering temperature and mass loss were generated. The correlation between the experimental mass loss and the 2-D model mass loss was derived using the simulated equivalent radius in the charred foam zone. The model reproduced the ranking of smoldering propensity by mass loss that was observed experimentally, and predicted that the mass loss at a foam thickness of 102 mm (about 4 inch) and above (as typically used in RUF) is always lower than ML_{MM2} and higher than ML_{SM2}. This result indicates that: (1) the standard mock-up with a 51 mm–thick foam, currently adopted to assess and regulate smoldering ignition resistance of residential upholstered furniture, is expected to underestimate smoldering in a RUF item, and; (2) the modified mock-up with a 51 mm–thick foam is expected to be a more robust predictor of smoldering in RUF that may offer a near-worst-case scenario, useful to identify the upholstery materials that prevent most smoldering ignitions independent of the construction and geometry of the actual furniture.

Acknowledgements

The authors are grateful to Morgan Bruns (Virginia Military Institute) and William M. Pitts (NIST) for valuable discussions and to Zhe Chen (NIST) for his contributions.

References

[1] Ohlemiller T.J. (2002) *Smoldering combustion.* SFPE handbook of fire protection engineering, **3**.

[2] Rein G. (2016) *Smoldering combustion*, SFPE Handbook of Fire Protection Engineering. Springer, New York, NY, pp 581-603.

[3] Zammarano M., Matko S., Krämer R.H., *et al.* (2012) *Smoldering in flexible polyurethane foams: the effect of foam morphology*. American Chemical Society, pp 459-479.

[4] Hall J.R. (2015) *Estimating fires when a product is the primary fuel but not the first fuel, with an application to upholstered furniture.* Fire Technology, **51**(2): 381-391.

[5] Ahrens M. (2008) *Home fires that began with upholstered furniture*. National Fire Protection Association Quincy, MA, USA. Available online on February 25, 2020 at: https://www.nfpa.org/-/media/Files/News-and-Research/Fire-statistics-and-reports/US-Fire-Problem/Fire-causes/osupholstered.pdf.

[6] *Filling/padding component test method-barrier test method-fabric classification test method.* (1990) Upholstered Furniture Action Council (UFAC).

[7] ASTM, *Standard E1353, standard test methods for cigarette ignition resistance of components of upholstered furniture.* ASTM Standards for Upholstered Furniture, Mattresses and Bedding. (2008) West Conshohocken, PA: ASTM International.

[8] NFPA 260 - *Standard methods of tests and classification system for cigarette ignition resistance of components of upholstered furniture.* Quincy, MA: National Fire Protection Association (NFPA).

[9] *Requirements, test procedure and apparatus for testing the flame and smolder resistance of upholstered furniture.* Technical Bulletin 117-2013, June 2013. North Highlands, CA: Bureau of Home Furnishings and Thermal Insulation. Department of Consumer Affairs, State of California.

[10] Loftus J.J. (1975) *Test Method for Classifying Cigarette Ignition Characteristics of Upholstery Furniture*, NBS report to CPSC, March 6, 1975. Available online on February 25, 2020 at: https://nvlpubs.nist.gov/nistpubs/Legacy/IR/nbsir78-1438.pdf.

[11] *116th Congress 1st Session-Safer Occupancy Furniture Flammability Act.* 2019.

[12] Damant G.H. (1995) *Cigarette ignition of upholstered furniture.* Journal of Fire Sciences, **13**(5): 337-349.

[13] Damant G.H. (1990) *Flammability of Soft Furnishings. What's Happening in California?* Journal of fire sciences, **8**(5): p. 313-330.

[14] *Upholstered furniture memoranda.* Bethesda, MD: U.S. Consumer Product Safety Commission, 2012. Available online on February 25, 2020 at: https://www.cpsc.gov/s3fs-public/ufmemos.pdf.

[15] Ohlemiller T.J., Bellan J., Rogers F. (1979) *A model of smoldering combustion applied to flexible polyurethane foams.* Combustion and Flame, **36**: 197-215.

[16]] Zammarano M., Matko S., Pitts W.M., *et al.* (2014) *Towards a reference polyurethane foam and bench scale test for assessing smoldering in upholstered furniture.* Polymer Degradation and Stability, **106**: 97-107.

[17] Leach S.V., Rein G., Ellzey J.L., *et al.* (2000) *Kinetic and fuel property effects on forward smoldering combustion.* Combustion and flame, **120**(3): 346-358.

[18] Rein G., Bar-Ilan A., Fernandez-Pello A.C., *et al.* (2005) *Modeling of one-dimensional smoldering of polyurethane in microgravity conditions.* Proceedings of the Combustion Institute, **30**(2): 2327-2334.

[19] Rein G., Fernandez-Pello A.C., Urban D.L., (2007) *Computational model of forward and opposed smoldering combustion in microgravity.* Proceedings of the Combustion Institute, **31**(2): 2677-2684.

[20] Ohlemiller T.J. (1985) *Modeling of smoldering combustion propagation.* Progress in Energy and Combustion Science, **11**(4): 277-310.

[21] Dodd A.B., Lautenberger C, Fernandez-Pello AC, (2009) *Numerical examination of two-dimensional smolder structure in polyurethane foam.* Proceedings of the Combustion Institute, **32**(2): 2497-2504.

[22] Gann R.G., and Hnetkovsky E.J., NIST Technical Note 1627 - *Modification of ASTM E 2187 for Measuring the Ignition Propensity of Conventional Cigarettes*. Available online on February 25, 2020 at: http://www.nist.gov/customcf/get_pdf.cfm?pub_id=902075.

[23] Yang J., Liu N., Chen H., *et al.* (2019) *Smoldering and spontaneous transition to flaming over horizontal cellulosic insulation.* Proceedings of the Combustion Institute, **37**(3): 4073-4081.

[24] Torero J.L., Fernandez-Pello A.C., Kitano M., (1993) *Opposed forced flow smoldering of polyurethane foam.* Combustion Science and Technology, **91**(1-3): 95-117.

[25] Torero J.L., Fernandez-Pello A.C., (1996) *Forward smolder of polyurethane foam in a forced air flow.* Combustion and Flame, **106**(1-2): 89-109.

[26] Middleman S. (1998) *An introduction to mass and heat transfer: principles of analysis and design.* European Journal of Engineering Education, **23**(3): 397.

[27] Holleyhead R. (1999) *Ignition of solid materials and furniture by lighted cigarettes. A review.* Science & Justice, **39**(2): 75-102.

[28] Baker, R.R. (1981) *Product formation mechanisms inside a burning cigarette.* Progress in Energy and Combustion Science, **7**(2): 135-153.

[29] Lock A. (2016) *Memoranda on Full-Scale Upholstered Furniture Testing, 2014-2015.* Retrieved from U.S. Consumer Product Safety Commission. Available online on February 25, 2020 at: https://cpsc.gov/s3fs-public/FY14_Chair_Study_Memos.pdf.

[30] Hamby D. (1994) *A review of techniques for parameter sensitivity analysis of environmental models.* Environmental monitoring and assessment, **32**(2): 135-154.

Appendix A

The one-at-a-time sensitivity analysis (only one parameter varies at a time while holding all the others as the base case values) [30] was used in the parametric study. Considering a large amount of model inputs (>40), here only the sensitivity to major kinetic parameters (see Table A1) that treated as independent variable x was examined.

Table A1. Major independent variables x in model

Parameters/*k*	***fp***	***fo***	***co***
A_k (s^{-1})	5×10^{15} $[1\times10^{15}, 10\times10^{15}]$	2×10^{12} $[1\times10^{12}, 10\times10^{12}]$	4×10^{13} $[1\times10^{13}, 10\times10^{13}]$
E_k (kJ mol^{-1})	200 [195, 205]	155 [150, 160]	185 [180, 190]
n_k (-)	3 [1,5]	-	-
ΔH_k (J g^{-1})	775 [500, 1000]	-900 [-1200, -500]	-4600 [-5000, -3500]

Two candidates of y_1, y_2 are selected as the dependent variable y. They are the peak smoldering temperature at $t = 15$ min and the time for the upward spread of foam oxidation front to reach the top of the vertical foam. For each candidate y_i, the sensitivity to the independent variable x is deduced by Eq. (A1). The upper (x_{up}) and lower (x_{low}) limits of independent variable x (x_0 is the base case value) are estimated in this work. The overall sensitivity of x is quantified by a weighted sensitivity coefficient (Eq. (A2)).

$$\Phi_i(x) = \sqrt{\left(\frac{|y_i(x_{\text{up}}) - y_i(x_0)|}{(x_{\text{up}} - x_0)} \cdot \frac{x_0}{y_i(x_0)}\right)^2 + \left(\frac{|y_i(x_{\text{low}}) - y_i(x_0)|}{|x_{\text{low}} - x_0|} \cdot \frac{x_0}{y_i(x_0)}\right)^2}\,,\ i=1, 2 \qquad \text{(A1)}$$

$$\bar{\Phi}(x) = \frac{1}{2}\sum_{i=1}^{2}\Phi_i(x) \qquad \text{(A2)}$$

In Fig. A1, a sensitivity ranking shows that the variation in chemical parameters of foam pyrolysis and foam oxidation (*i.e.* E_{fp}, E_{fo}) are more influential on smoldering combustion, compared to that of char oxidation. The activation energy of foam pyrolysis and foam oxidation, and the pre-exponential factor of foam pyrolysis reaction are the most three dominant parameters affecting smoldering combustion in SM3, while in MM3, the sensitivity to char oxidation improves due to the enhanced oxygen supply.

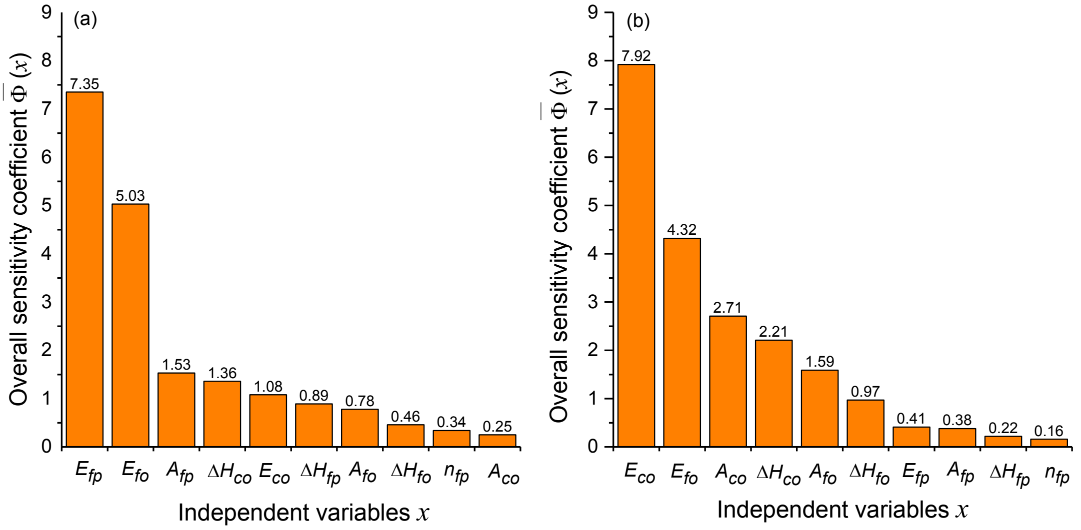

Fig. A1. Overall sensitivity coefficient $\overline{\Phi}(x)$ of the chemical parameters used in the (a) SM3 (b) MM3.

Fig. A2. Post-test photograph of the charred foam removed from the mock-up.

Supplemental information

1. Standard mock-up with 76 mm-thick foam (SM3)

Fig. S1 displays the simulated results of temperature, bulk density of the foam component, the mass fraction of oxygen and the rates of reaction along the mid-section of the vertical foam at representative selected times (*i.e.*, 30 min, 38.5 min, 45 min and 60 min) in SM3.

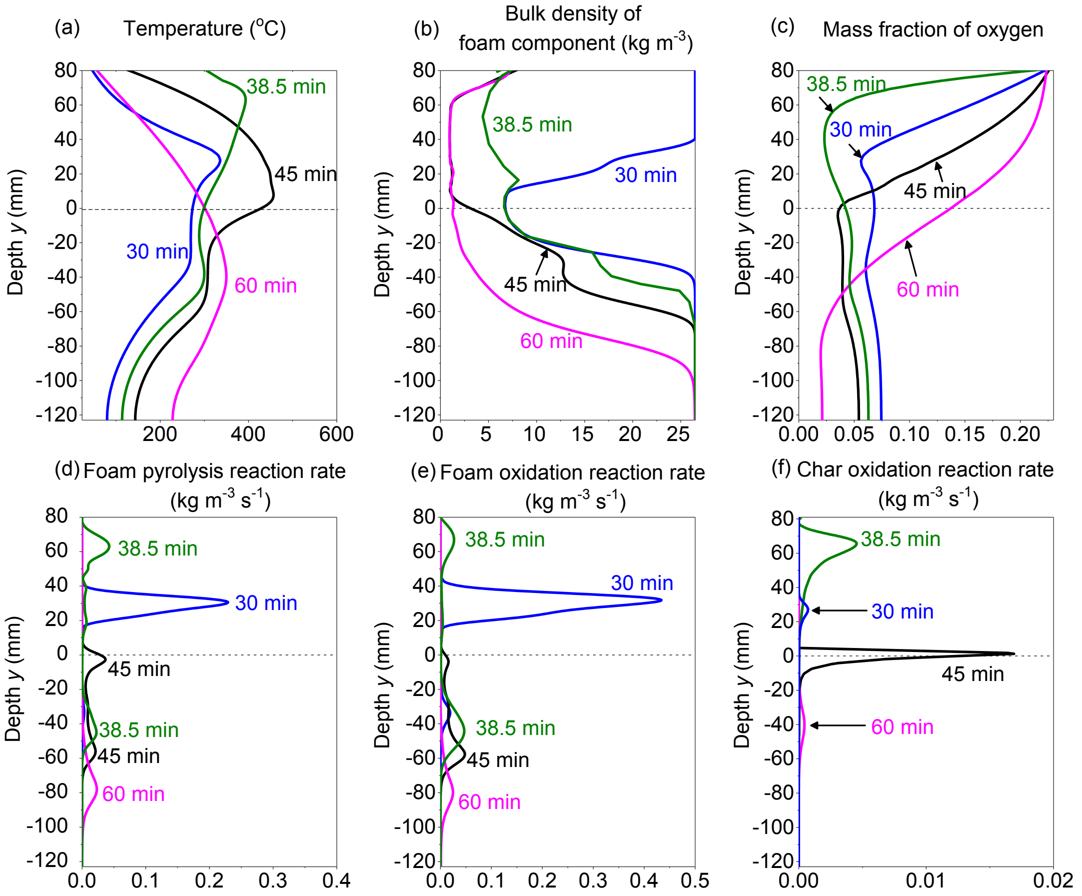

Fig. S1. Simulated profiles of (a) temperature, (b) bulk density of foam component, (c) mass fraction of oxygen, (d) foam pyrolysis rate, (e) foam oxidation rate, (f) char oxidation reaction rate along the mid-section of the vertical foam in SM3.

In Fig S1a, modelling results show two local maxima for temperature that moves from $y \approx 28$ mm and $y \approx -30$ mm at $t = 30$ min to $y \approx 65$ mm and $y \approx -45$ mm, respectively, at $t = 38.5$ min. Assuming that these local temperature maxima can be used to track the position of the smoldering front [17], these results hints to the simultaneous generation of an upward smoldering wave and a downward smoldering wave between $t = 0$ min and $t = 38.5$ min. The local maxima at $y \approx 5$ mm for $t = 45$ min suggests that this upward smoldering wave ends after reaching the top of the foam at $t = 38.5$ min, and a second downward wave is generated. Meanwhile, the first downward smoldering wave keeps propagating further down into the foam until $t = 60$ min.

Fig. S1b shows that the bulk density of the foam component is reduced from 26.5 kg m^{-3} at $t = 0$ min to about 5 kg m^{-3} at $t = 38.5$ min by the first upward and downward waves, and then further reduced to about 1 kg m^{-3} at $t = 60$ min by the second downward wave.

Fig. S1c indicates that oxygen is almost fully depleted in the bottom region (oxygen mass fraction drops from a value of 0.23 in air to a value that ranges between 0.03 and 0.07 at $t = 30$ min, 38.5 min and 45 min), and oxygen concentration rapidly increases in the upper region. During the propagation of the second wave ($t = 60$ min), the oxygen concentration decreases even further down to a minimum value of about 0.02 for $y < -80$ mm.

Figs. S1d, S1e, S1f shows the reaction rates for foam pyrolysis, foam oxidation and char oxidation. The simulations indicate that the upward smoldering wave is mainly due to a combination of a foam pyrolysis wave followed, shortly after, by a foam oxidation wave (see foam pyrolysis and foam oxidation peaks at $y \approx 30$ mm for $t = 30$ min). The distance between the pyrolysis and the oxidation waves (as indicated by their respective peaks in reaction rates) in this upward smoldering wave is in the order of 1 mm. The first downward smoldering wave is also due to the combination of foam pyrolysis and foam oxidation, but the rates of reactions are much lower as compared to the ones observed for the upward smoldering wave (see foam pyrolysis and foam oxidation peaks at $y \approx -35$ mm for $t = 30$ min) due to oxygen depletion. In the lower region ($y < 0$), the foam oxidation due to the first upward smoldering wave depletes oxygen so that the rate of the first downward wave is suppressed. In the upper region ($y > 0$), the second downward wave due to char oxidation is not activated until the first wave ceases and reaches the top of the foam at $t = 38.5$ min. A sharp and intense peak in char oxidation is generated at $t = 45$ min (Fig. 4f) and causes a substantial increase in peak smoldering temperature (Fig. S1a). Meanwhile, in the lower region ($y < 0$), the first downward wave keeps propagating downward. At $t = 60$ min, the second downward front catches up with the first downward front in the lower region, leaving only a single reaction rate peak (Figs. S1d and S1e). The oxygen supply gradually decreases with the smoldering front approaching the bottom of the foam. As a result, the char oxidation rate decreases from 1.67×10^{-2} kg m^{-3} s^{-1} at $y = 2$ mm after 45 min to 4.5×10^{-4} kg m^{-3} s^{-1} at $y = -40$ mm after 60 min (Fig. S1f).

2. Modified mock-up with 76 mm-thick foam (MM3)

Fig. S2 displays the simulated profiles of temperature, bulk density of foam component, mass fraction of oxygen and each reaction rate along the mid-section of the vertical foam in MM3.

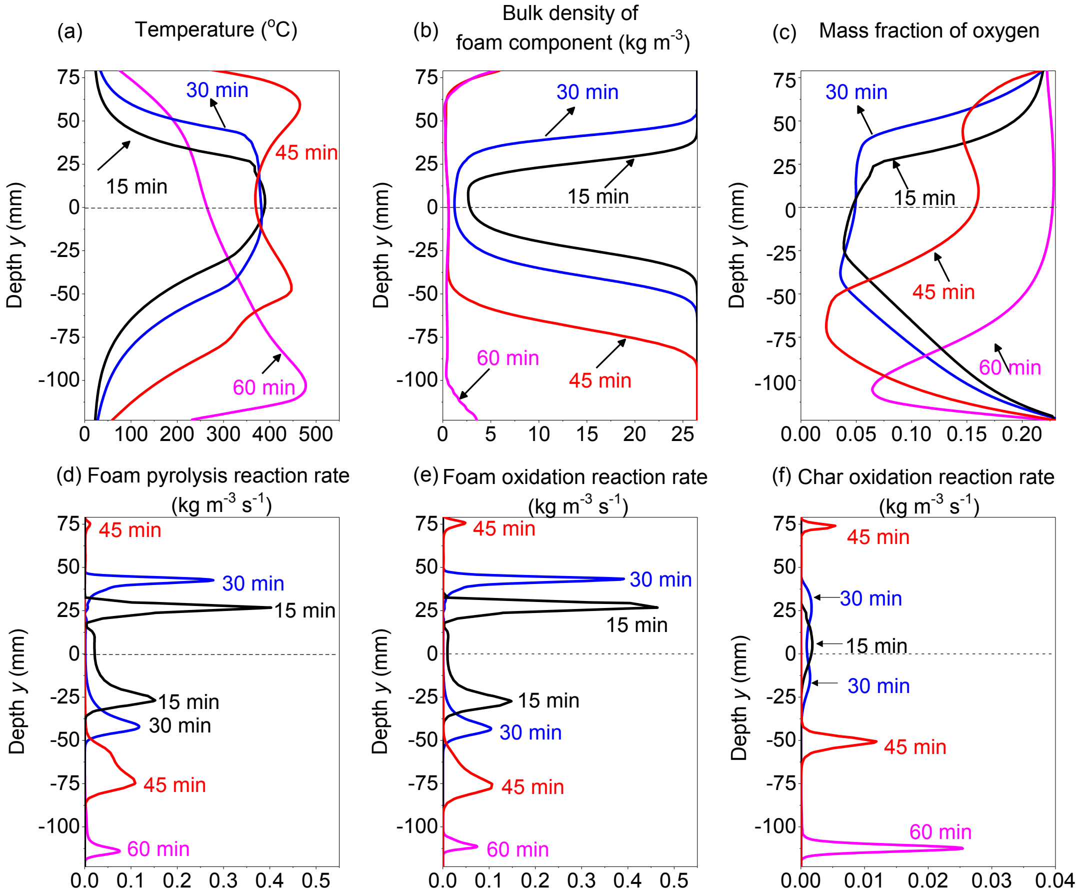

Fig. S2. Simulated profiles of (a) temperature (b) bulk density of foam component (c) mass fraction of oxygen and (d) foam pyrolysis (e) foam oxidation (f) char oxidation reaction rates along the centerline of the vertical foam in MM3.

At t = 15 min, a plateau smoldering temperature of ~360 °C is generated between $y \approx$ -25 mm to $y \approx$ 25 mm (Fig. S2a). At t = 30 min, this temperature plateau extends to $y \approx$ -40 mm and $y \approx$ 40 mm. Thereafter (see Figs. S2a at t = 45 min), the initial broad temperature plateau splits into two sharper and higher temperature peaks. At t = 45 min, the peak smoldering temperature increases to about 465 °C at $y \approx$ 60 mm and to 445 °C at $y \approx$ -50 mm, and to about 490 °C at $y \approx$ 110 mm at t = 60 min. These results hints to the simultaneous generation of an upward smoldering wave and a downward smoldering wave between t = 0 min and $t \approx$ 45 min, and the generation of a second downward smoldering at $t \approx$ 45 min that catches up with the first downward smoldering wave by t = 60 min.

This smoldering scenario is further supported by the reaction rates for foam pyrolysis, foam oxidation and char oxidation (Figs. S2d, S2e, and S2f). At t = 15 min and t = 30 min two distinct peaks for foam oxidation/pyrolysis are observed; the upper peaks move upward whereas the lower peaks move downward. These two smoldering waves (one upward and one downward) are due to the combination of foam pyrolysis and foam oxidation.

At $t = 45$ min, the oxidation/pyrolysis peaks (upward wave) approach the top of the foam and two char oxidation peaks (downward waves) are generated at $y \approx 70$ mm and $y \approx - 55$ mm. At $t = 60$ min, only a single peak for foam oxidation/pyrolysis and char oxidation are observed.

Figs. S2d, S2e, and S2f show that at $t = 15$ min and $t = 30$ min the magnitudes of foam pyrolysis and foam oxidation reaction rate are comparable, but in comparison with the char oxidation reaction rate, are one-order magnitude higher. Hence, smoldering is initially dominated by foam pyrolysis and foam oxidation. Thereafter (see Figs. S2d, S2e, and S2f at $t = 45$ min and $t = 60$ min), the magnitude of char oxidation becomes higher than the magnitudes of foam pyrolysis and foam oxidation reaction. The intense char oxidation peak at $t = 60$ mm causes an increase in temperature up to about 490 °C at $y \approx 110$ mm (Fig. S2a). The foam component is almost consumed (Fig. S2b) and the mass fraction of oxygen decreases to less than 5% (Fig. S2c) between $y = - 40$ mm and $y = 40$ mm.

Compared to SM3, the char oxidation and foam oxidation rates in the lower region are significantly higher in MM3. This is because oxygen depletion in proximity of the bottom of the mock-up ($y < - 100$ mm) is observed in SM3 but not MM3 (see Fig. S1c and Fig. S2c).